Inverse oculomotor responses of achiasmatic mice expressing a transfer-defective Vax1 mutant

Kwang Wook Min[1], Namsuk Kim[1,2], Jae Hoon Lee[3], Younghoon Sung[4], Museong Kim[1], Eun Jung Lee[1], Jae-Hyun Kim[1], Jaeyoung Lee[1], Jong-Myeong Kim[1], Jee Myung Yang[5], Seung-Hee Lee[1], Han-Woong Lee[3], and Jin Woo Kim[1,6]

[1] Department of Biological Sciences, Korea Advanced Institute of Science and Technology (KAIST), Daejeon, South Korea

[2] Neurovascular Unit, Korea Brain Research Institute (KBRI), Daegu, South Korea

[3] Department of Biochemistry, College of Life Science and Biotechnology, Yonsei University, Seoul, South Korea

[4] Department of Convergence Medicine, University of Ulsan College of Medicine, Seoul, South Korea

[5] Department of Ophthalmology, Asan Medical Center, University of Ulsan College of Medicine, Seoul, Korea.

[6] Corresponding author and lead contact: Jin Woo Kim (jinwookim@kaist.ac.kr)

Key words: ventral anterior homeobox (Vax1), optic chiasm, optic stalk, homeodomain protein transfer, oculomotor response

ABSTRACT

In animals that exhibit stereoscopic visual responses, the axons of retinal ganglion cells (RGCs) connect to brain areas bilaterally by forming a commissure called the optic chiasm (OC). Ventral anterior homeobox 1 (Vax1) contributes to formation of the OC, acting endogenously in optic pathway cells and exogenously in growing RGC axons. Here, we generated *Vax1*$^{AA/AA}$ mice expressing the Vax1^{AA} mutant, which is selectively incapable of intercellular transfer. We found that RGC axons cannot take up Vax1^{AA} protein from *Vax1*$^{AA/AA}$ mouse optic stalk (OS) cells, of which maturation is delayed, and fail to access the midline. Consequently, RGC axons of *Vax1*$^{AA/AA}$ mice connect exclusively to ipsilateral brain areas, resulting in the loss of stereoscopic vision and the inversed oculomotor responses. Together, our study provides physiological evidence for the necessity of intercellular transfer of Vax1 and the importance of the OC in binocular visual responses.

INTRODUCTION

Animals collect visual information via the eyes, where photoreceptors in the retina convert light stimuli to electrochemical signals (Seabrook et al., 2017). These signals are then transmitted to inner retinal neural circuits before being sent to the brain via the axons of retinal ganglion cells (RGCs). RGC axons, which are bundled in the optic nerve, deliver visual information to multiple brain areas, including the dorsal lateral geniculate nucleus (dLGN) of the thalamus, for pattern and color recognition; the superior colliculus (SC) of the midbrain, for oculomotor responses; and the suprachiasmatic nucleus (SCN) of the hypothalamus, for circadian rhythm control (Rusak and Groos, 1982; Seabrook et al., 2017; Zhang et al., 2017).

In many binocular animals, RGC axons are not only wired to brain areas on the same (i.e., ipsilateral) side but are also connected to those on the opposite (i.e., contralateral) side (Herrera et al., 2019; Petros et al., 2008). The population of RGCs whose axons project to contralateral brain areas is variable among vertebrate species. Human RGC axons are split equally to both sides at the midline, whereas all RGC axons in *Xenopus laevis* and zebrafish extend exclusively to the contralateral side across the midline (Herrera et al., 2019; Petros et al., 2008). In mice, the population of RGCs that connects to ipsilateral brain areas is low: ~3% in pigmented mice and ~1% in albino mice (Rice et al., 1995).

RGC axons form a midline structure called the optic chiasm (OC), which is located beneath the SCN and splits the axon bundles into ipsilateral and contralateral paths (Herrera et al., 2019; Petros et al., 2008). Pathway selection for RGC axons at the OC is determined by specific guidance cues. For example, ephrin B2 and B3 expressed in radial glia of the ventral hypothalamus (vHT) act through a receptor, EphB1, in RGC axons from the ventral temporal retina to repel the axons from the midline, guiding their growth ipsilaterally (Williams et al., 2003). EphB1 is present in about 50% of human RGCs and ~3% mouse RGCs, but is absent in *Xenopus* and zebrafish RGCs, suggesting a critical role for

EphB1 in ipsilateral pathway selection by RGC axons (Herrera et al., 2003; Rebsam et al., 2012). Pathway-selection cues are not only provided by cells located along RGC axon growth tracks, but also by neighboring RGC axons. Sonic hedgehog (Shh), which is expressed in contralaterally projecting RGC axons, also serves as a repulsive cue in the OC by acting on its co-receptor, Boc, which is expressed in RGC axons from the ventral temporal mouse retina (Peng et al., 2018).

The cues that guide the majority of mouse RGC axons across the midline, however, have not been identified as clearly as the ipsilateral guidance cues. Binding of vascular endothelial growth factor-a (Vegfa) to its receptor, neurophilin-1 (Nrp1), has been demonstrated to support the growth of RGC axons at the midline (Erskine et al., 2011). Homophilic interactions between neuronal cell adhesion molecule (Nr-CAM) expressed in RGC axons and vHT cells has also been suggested to promote midline crossings of RGC axons (Williams et al., 2006). Nr-CAM also cooperates with plexinA1, a receptor for semaphorin 6D (Sema6D), to support contralateral RGC axon projection (Kuwajima et al., 2012). However, a majority of RGC axons still cross the midline in mice lacking these cues, suggesting the presence of other key regulator(s) of contralateral RGC axon growth.

Ventral anterior homeobox 1 (Vax1) is expressed in ventral and medial regions of the vertebrate forebrain (Bertuzzi et al., 1999; Hallonet et al., 1999). The forebrain commissural structures, including the anterior commissure (AC), corpus callosum (CC), hippocampal commissure (HC), and OC, do not form properly in humans and mice having homozygous *VAX1* mutations (Bertuzzi et al., 1999; Mui et al., 2005; Slavotinek et al., 2012). Given the absence of *VAX1* gene expression in commissural neurons, it had been thought that Vax1 functions as a transcription factor that induces axon growth factors in cells located along commissural axon growth tracks. However, it was found that the transcription factor activity of Vax1 is dispensable for the promotion of mouse RGC axon growth (Kim et al., 2014). More surprisingly, Vax1 protein was detected in mouse RGC axons, despite the absence of autonomous *Vax1* gene expression in RGCs (Kim et al., 2014). It was further found that Vax1 protein is transferred from cells along RGC axon

growth tracks and promotes axon growth by stimulating axonal mRNA translation in mouse retinal explants (Kim et al., 2014). However, whether intercellular Vax1 transfer is also critical for the growth of RGC axons *in vivo* has been remained unclear.

Here, we generated *Vax1*$^{AA/AA}$ mice, in which the *Vax1* was replaced with a transfer-defective *Vax1*^{AA} mutant. We found that Vax1^{AA} protein was incapable of binding to heparan sulfate proteoglycans (HSPGs) and penetrating RGC axons, resulting in retarded growth of RGC axons. Most of all, the OC was not formed in *Vax1*$^{AA/AA}$ mutant mice, and RGC axons projected exclusively to ipsilateral brain areas. Consequently, *Vax1*$^{AA/AA}$ mice exhibited inversed oculomotor behaviors, resulting from ipsilaterally biased retinogeniculate and retinocollicular connections in opposing to those of the contralateral-dominant connections in *Vax1*$^{+/+}$ mice. Our findings in *Vax1*$^{AA/AA}$ mice, therefore, not only confirm the physiological importance of Vax1 transfer in OC formation but also provide a molecular basis for the oculomotor abnormalities seen in achiasmatic animals.

RESULTS

Identification of a CAG sugar-binding motif in Vax1

Vax1 is secreted from cells that interact with developing mouse RGC axons and enters into the axons. Binding of Vax1 to RGC axons is mediated by heparan sulfate (HS) sugar chains of HSPGs, such as syndecan (Sdc) and glypican (Glp) (Kim et al., 2014). Another homeodomain protein, Otx2 (orthodenticle homeobox 2), has been found to bind chondroitin sulfate (CS) sugar chains of chondroitin sulfate proteoglycan (Beurdeley et al., 2012; Miyata et al., 2012). Binding of Otx2 to CS was mediated by the conserved glycosaminoglycan (GAG) binding motifs, [-X-B-B-X-B-X-] and [-X-B-B-B-X-X-B-X-] (Cardin and Weintraub, 1989).

We found mouse Vax1 also contains a GAG-binding motif located at amino acids 100–105 (Figure 1A). To investigate the possibility that Vax1 binds to HS chains through this putative CAG-binding motif, we replaced lysine and arginine (KR) amino acid residues in the motif to two alanines (A), yielding Vax1^{AA} (Figure 1A). HeLa cells were transfected with DNA construct that expresses a mRNA containing Vax1 or mutant Vax1^{AA} together with enhanced green fluorescent protein (EGFP) but produces EGFP separately from Vax1 or Vax1^{AA} using an internal ribosome entry site (IRES). The KR-to-AA mutation suppressed Vax1 transfer from EGFP-positive donor cells to EGFP-negative recipient cells (Lee et al., 2019) (Figure 1B). However, it did not significantly affect Vax1 transcription factor activity, assessed by monitoring the expression of a luciferase reporter downstream of a Vax1 target sequence in the intron 5 of *transcription factor 7-like 2* (*Tcf7l2*) (Vacik et al., 2011) (Figure 1C). This finding contrasts with the reduced transcription factor activity of the Vax1^{R152S} mutant (Figure 1C), in which arginine 152 (R152) of the DNA binding motif was mutated to serine (S) (Slavotinek et al., 2012).

We found that the level of Vax1^{AA} protein in growth media of the transfected cells was significantly elevated compared with that of Vax1 (Figure 1D). However, the amount of Vax1^{AA} in the medium was not further increased by the addition of free heparin, which competes with HS chains of HSPGs to bind extracellular Vax1 and release it from the cell surface into the growth medium (Lee et al., 2019) (Figure 1D). The results suggest reduced affinity of Vax1^{AA} for HS sugars compared with Vax1, together with a result that shows the impaired interaction between Vax1^{AA} and syndecan-2 (Sdc2) HSPG (Figure 1E). Consequently, Vax1^{AA} added to growth medium bind or penetrate HeLa cells much less efficiently than Vax1 (Figure 1F).

We further tested whether the KR-to-AA mutation also influences the binding of Vax1 to RGC axons and subsequent axon growth stimulation. We found that Vax1^{AA} protein added into the growth medium of mouse retinal explants was not detected in neurofilament 160 (Nf160)-positive RGC axons nor did it induce axonal growth as efficiently as Vax1 protein, which penetrated retinal axons and significantly promoted

axonal growth (Figure 1G). We also found that Vax1^{AA} was not transferred to RGC axons from human embryonic kidney 293T cells co-cultured with mouse retinal explants (Figure 1H). Consequently, the lengths of RGC axons extending toward Vax1^{AA}-expressing 293T cells were shorter than those growing towards Vax1-expressing 293T cells. These results suggest that the KR residues are necessary for the binding of Vax1 to HSPGs and subsequent penetration into RGC axons.

Generation of Vax1$^{AA/AA}$ mice

To investigate the consequences of the KR to AA mutation *in vivo*, we introduced the corresponding mutation into the mouse *Vax1* gene and generated *Vax1^{AA}* mice (Figure S1A and S1B; see Methods for details). *Vax1$^{AA/AA}$* homozygous mice were born without any recognizable morphological defects and survived without significant health problems, whereas the mice carry homozygous non-sense mutations (*Vax1$^{-/-}$*) or hemizygous KR-to-AA mutation together non-sense mutation (*Vax1$^{AA/-}$*) die after birth with the cleft palates that interfere with breathing (Bertuzzi et al., 1999) (Figure S1C – S1E). Noticeably, the incisors grow continuously in approximately a quarter of *Vax1$^{AA/AA}$* mice (Figure S1D). The outgrowing incisors make the mice difficult to consume chow and cause a lethality after weaning, unless the outgrown incisors were not cut off regularly (Figure S1E).

Using *Vax1$^{AA/AA}$* mouse embryos, we examined whether the mutation affects intercellular transfer of Vax1 *in vivo*. We found Vax1^{AA} was strongly expressed in ventral medial forebrain structures, including the optic stalk (OS) of *Vax1$^{AA/AA}$* mouse embryos at 14.5 days post-coitum (dpc; E14.5), an expression pattern similar to that of Vax1 in E14.5 *Vax1$^{+/+}$* littermate mice (Figure 1I). However, unlike the distribution of Vax1, which was present in RGC axons as well as OS cells in *Vax1$^{+/+}$* mice, Vax1^{AA} was not detectable in the RGC axons of *Vax1$^{AA/AA}$* mice (Figure 1I). These results suggest that the KR-to-AA mutation also interferes with the transfer of Vax1 to RGC axons *in vivo*.

Delayed maturation of the OS in Vax1$^{AA/AA}$ mice

A coloboma, the fissures in the ventral eyecup and OS, is observed in the eyes of humans and mice harboring *VAX1* mutations (Bertuzzi et al., 1999; Hallonet et al., 1999; Slavotinek et al., 2012). A coloboma was also present in E14.5 *Vax1*$^{AA/AA}$ and *Vax1*$^{-/-}$ mouse eyes (Figure 2A [top row] and 2B). The optic fissures, however, disappeared in *Vax1*$^{AA/AA}$ mice by E16.5, whereas they remained unclosed in *Vax1*$^{-/-}$ mice even after birth (Figure 2A [middle row] and 2B). The unclosed OS in E14.5 *Vax1*$^{AA/AA}$ mice expressed Pax2 (paired homeobox 2), an OS marker, but not Pax6, a retinal marker, similar to the distribution observed in *Vax1*$^{+/+}$ littermates (Figure 2C [coronal], left and center columns). It contrasts with E14.5 *Vax1*$^{-/-}$ mice, which co-expressed Pax2 and Pax6 in the OS (Figure 2C [coronal], right column). Therefore, these results suggest that OS fate is specified properly in *Vax1*$^{AA/AA}$ mice, but not in *Vax1*$^{-/-}$ mice.

Pax2-positive OS cells were clustered separately from RGC axons in E14.5 *Vax1*$^{AA/AA}$ and *Vax1*$^{-/-}$ mice, whereas they were spread among RGC axons in E14.5 *Vax1*$^{+/+}$ mice (Figure 2C, sagittal). The OS cells in E14.5 *Vax1*$^{+/+}$ mice expressed an astrocyte precursor cell (APC) marker, S100 calcium-binding protein ß (S100ß), but had lost a neuroepithelium marker, E-cadherin (Ecad) (Figure 2D, left column of E14.5 panel). The ventral OS (vOS) cells in E14.5 *Vax1*$^{AA/AA}$ mice also expressed S100 without Ecad, however their dOS cells co-expressed Ecad and S100ß (Figure 2D, center column of E14.5 panel). However, S100ß was undetectable in E14.5 *Vax1*$^{-/-}$ mouse vOS cells, which instead expressed the retinal marker Vsx2 (Figure 2D, right column of E14.5 panel). In E16.5 *Vax1*$^{AA/AA}$ mice, similar to the distribution observed in *Vax1*$^{+/+}$ littermates, S100ß-positive OS APCs had entirely lost Ecad expression and started to disperse among RGC axons, whereas S100ß-negative OS cells still formed Ecad-positive neuroepithelial clusters in E16.5 *Vax1*$^{-/-}$ mice (Figure 2D, E16.5 panel). These results suggest that

differentiation of APCs from the OS neuroepithelium is impaired in *Vax1*$^{-/-}$ mice but merely delayed in *Vax1*$^{AA/AA}$ mice.

Agenesis of the OC in Vax1*$^{AA/AA}$ *mice

The APCs and RGC axons were segregated from each other throughout the entire OS in E14.5 *Vax1*$^{AA/AA}$ mice (Figure 3A and 3B, center columns in HT/OS junction panels). These naked RGC axons in *Vax1*$^{AA/AA}$ mice failed to cross the vHT midline, whereas RGC axons in *Vax1*$^{+/+}$ littermates were intercalated by Vax1-positive OS cells and formed the OC at the vHT midline (Figure 3A and 3B, left columns in HT/OS junction and OC panels). However, RGC axons were able to form the optic tract (OT) along the lateral wall of post-chiasmatic brain region of E14.5 *Vax1*$^{AA/AA}$ mice (Figure 3A and 3B, center columns in OT panels). RGC axons of E14.5 *Vax1*$^{-/-}$ mice also failed to extend to the vHT midline but could form the OT (Figure 3A and 3B, right columns in OC and OT panels), as it was reported previously (Bertuzzi et al., 1999).

The vHT of E14.5 *Vax1*$^{AA/AA}$ and *Vax1*$^{-/-}$ mice protruded ventrally by virtue of the absence of underlying RGC axons bundles, while the vHT of E14.5 *Vax1*$^{+/+}$ mice was flattened over RGC axons forming the OC (Figure 3A, OC panel). However, sonic hedgehog (Shh), which is necessary for specification of the vHT and OS (Chiang et al., 1996; Kim and Lemke, 2006), showed a similar expression pattern in the vHTs of E14.5 *Vax1*$^{+/+}$, *Vax1*$^{AA/AA}$ and *Vax1*$^{-/-}$ mice (Figure 3C, top row), suggesting that fate specification of the vHT is unaffected in *Vax1*$^{AA/AA}$ and *Vax1*$^{-/-}$ mice. The Glast-positive radial glia, which express various RGC axon guidance cues (Herrera et al., 2019; Petros et al., 2008), were also observed in vHT of *Vax1*$^{AA/AA}$ and *Vax1*$^{-/-}$ mice, suggesting normal development of vHT radial glia from Nestin-positive vHT neuroepithelium in the mice (Figure 3C, second and third rows).

Attractive guidance cues for RGC axons, including Vegfa and Nr-Cam (Erskine et al., 2011; Williams et al., 2006), were expressed properly in the vHT of E14.5 *Vax1*$^{AA/AA}$ and *Vax1*$^{-/-}$ mice, although their expression pattern is not identical to those in the vHT of *Vax1*$^{+/+}$ littermates owing to ventral protrusion of HTs in *Vax1*$^{AA/AA}$ and *Vax1*$^{-/-}$ mice (Figure 3D, second and third rows). EphrinB2, which triggers the repulsion of ipsilaterally projecting RGC axons at the vHT midline (Williams et al., 2003), was not observed in the vHT of E14.5 *Vax1*$^{AA/AA}$ and *Vax1*$^{-/-}$ mice (Figure 3D, first row), suggesting the absence of ephrinB2-dependent repulsive signaling to RGC axons. However, EphB1, which binds ephrinB2 to promote retraction of RGC axons, and its upstream transcription factor Zic2 were detectable in ventral temporal RGCs of E14.5 *Vax1*$^{+/+}$, *Vax1*$^{AA/AA}$, and *Vax1*$^{-/-}$ mice (Herrera et al., 2003; Williams et al., 2003) (Figure 3E, top four rows). Shh, which was identified to repulse adjacent ventral temporal RGC axons from the vHT midline (Peng et al., 2018), was also expressed properly in RGCs (Figure 3E, bottom row). These results suggest that the agenesis of the OC in *Vax1*$^{AA/AA}$ mice did not likely result from the loss of attractive and/or gain of repulsive signals listed above.

Intact transcription factor activity of Vax1$^{AA/AA}$ in vivo

Our results indicate normal specification of OS and vHT but delayed differentiation of OS APC in *Vax1*$^{AA/AA}$ mice, of which RGC axons fail to form the OC (Figure 3F). The delayed maturation of OS cells in *Vax1*$^{AA/AA}$ mice could have resulted from autonomous alteration of gene expression, if the KA-to-AA mutation altered Vax1 transcription factor activity sufficiently to create a difference *in vivo* despite minimally affecting transcription factor activity in cultured cells (Figure 1B). We, thus, compared the activities of Vax1 and Vax1^{AA} *in vivo* by monitoring the expression of reporters driven by *Pax6* α-enhancer, where Vax1 binds to suppress the enhancer activity (Mui et al., 2005) (Figure 4A, diagram). We used α*-Cre;R26*^{tm11} mice, which express histone H2B-GFP (H2B-GFP) and membrane bound tdTomato (tdTom*) reporters at *ROSA26* gene locus upon the excision of *loxP-STOP-loxP*

(*LSL*) cassette by Cre recombinase expressed at downstream of *Pax6* α*-enhancer* (Marquardt et al., 2001; Wang et al., 2019) (Figure 4A, diagram). The H2B-GFP signals were observed only in the retina, but not in the OS, of E12.5 *Vax1*$^{+/+}$ and *Vax1*$^{AA/AA}$ littermate mice (Figure 4A), suggesting that Vax1 and Vax1^{AA} suppressed *Pax6* α-enhancer successfully in the OS.

We also compared the abilities of Vax1 and Vax1^{AA} to bind *Pax6* α-enhancer sequences *in vivo*. DNA fragments isolated from E10.5 mouse heads by chromosome immunoprecipitation (ChIP) using an anti-Vax1 antibody and used for polymerase chain reaction (PCR) and quantitative PCR (qPCR) detection of *Pax6* α-enhancer sequences in the ChIPed DNA. The results revealed no significant difference in the binding abilities of Vax1 and Vax1^{AA} on the target sequences (Figure 4B and 4C). Therefore, our results suggest that the delayed maturation of the OS in *Vax1*$^{AA/AA}$ mice is unlikely resulted from autonomous alteration of Vax1-dependent target gene expression.

Restoration of RGC axon growth in Vax1$^{AA/AA}$ mice by external supplementation of Vax1 protein

In *Vax1*$^{+/+}$*;*α*-Cre;R26*^{tm11} and *Vax1*$^{AA/AA}$*;*α*-Cre;R26*^{tm11} mice, we could also visualize RGC axons using tdTom* reporter (Figure 3A, diagram). After comparing the lengths of tdTom*-labeled RGC axons, we found RGC axon extension was less efficient in E12.5 *Vax1*$^{AA/AA}$ mice than that in *Vax1*$^{+/+}$ littermates (Figure 3A, arrowheads). Given the fact that exogenous Vax1 is capable of stimulating RGC axon growth (Kim et al., 2014), it is possible that the impaired RGC axon growth in *Vax1*$^{AA/AA}$ mice might be related to the absence of Vax1 in the axons (Figures 1F and 3B). We thus tested whether RGC axon growth in the OS and HT of *Vax1*$^{AA/AA}$ mice could be restored by supplying Vax1 protein exogenously. To this end, we implanted the third ventricle (V3) of E12.5 *Vax1*$^{AA/AA}$ mouse brain slabs with collagen beads that had been soaked in a solution containing recombinant

Flag-Vax1 proteins or Flag-peptides for 12 hours (Figure 4C; see details in Methods). We could detect Flag-Vax1 proteins in L1-CAM-positive RGC axons (Figure 4C, bottom row), which could be also identified by intraocularly-delivered lipophilic DiI fluorescent dye (Figure 4C, diagram). We further found an increase of DiI-labeled axons in the vHT midline of Vax1-implanted slabs in comparing with Flag peptide-implanted slabs (Figure 4C, second row). Some axons grew even farther across the midline, suggesting that exogenous Vax1 is necessary for the extension of RGC axons to form the OC.

Ipsilaterally biased RGC projections in the Vax1^{AA} mouse brain

Using adult *Vax1*$^{AA/AA}$ mice, we were able to analyze the structures and functions of the mouse visual system, which are difficult to study in *Vax1*$^{-/-}$ mice because they die perinatally (Bertuzzi et al., 1999). We found no significant difference in brain size and shape between P30 *Vax1*$^{+/+}$ and *Vax1*$^{AA/AA}$ littermate mice (Figure 5A and 5C [left column]). The olfactory bulb (OB) of *Vax1*$^{AA/AA}$ mice also appeared normal (Figure 5C, the image in left bottom corner), although a previous report noted hypoplastic OBs in the few surviving *Vax1*$^{-/-}$ mice (Soria et al., 2004). Furthermore, *Vax1*$^{AA/AA}$ mice have only one pituitary gland (data not shown), whereas *Vax1*$^{-/-}$ mice have an extra pituitary gland by virtue of failure to suppress ectopic pituitary fate specification in the ventral anterior forebrain (Bharti et al., 2011). These results also suggest that Vax1-dependent specification of ventral forebrain structures is not significantly altered in *Vax1*$^{AA/AA}$ mice.

Among the commissures that are reported to be absent in *Vax1*$^{-/-}$ mice (Bertuzzi et al., 1999), the CC and OC are missing in *Vax1*$^{AA/AA}$ mice, whereas the AC and HCC are present (Figure 5A and 5C [left column]). The posterior commissure (PC), where the oculomotor nerves (ON) cross the midline (Buuttner et al., 2002), was also present and appropriately positioned beneath the SC in *Vax1*$^{AA/AA}$ mice (Figure 5A, rightmost column). We further visualized the RGC axons of mice using fluorescent dye-conjugated cholera toxin B (CTB) protein (Luppi et al., 1990). The Alexa Fluor 488-conjugated CTB and Alexa

Fluor 594-conjugated CTB were injected into the right and left eyes, respectively, of *Vax1*$^{+/+}$ and *Vax1*$^{AA/AA}$ littermate mice at postnatal day 28 (P28; Figure 5B). Fluorescence signals emitted by CTB-labeled RGC axons in the mice were then detected at P30 (Figure 5C). Green and red fluorescence signals were predominantly detected in RGC axons that projected across the midline in *Vax1*$^{+/+}$ mice (Figure 5C, top row). Consequently, the majority of CTB fluorescence signals were observed in the contralateral SCs of *Vax1*$^{+/+}$ mice (Figure 5C, third row). In contrast, fluorescence signals of CTB were detected exclusively in the ipsilateral SCs of *Vax1*$^{AA/AA}$ mice, in which it was not possible to detect the OC where differentially labeled RGC axons met (Figure 5C, second and bottom rows).

We also examined whether ipsilaterally projecting *Vax1*$^{AA/AA}$ mouse RGC axons were properly connected to the dLGN, a thalamic nucleus that relays visual information from the retina to the visual cortex (Seabrook et al., 2017). Axons from RGCs in the ventral-temporal mouse retina project to the ipsilateral dLGN, where the majority of RGC axons from the contralateral retina are connected (Herrera et al., 2019; Petros et al., 2008). The minor ipsilateral axon terminals are then segregated from the major contralateral axon terminals by a retinal activity-dependent refinement process during postnatal development (Guido, 2018; Huberman et al., 2008). Segregation of binocular RGC axons was clearly seen in the dLGN of P30 *Vax1*$^{+/+}$ mice (Figure 5D, left two columns). However, RGC axons in the dLGN of P30 *Vax1*$^{AA/AA}$ mice originated only from the ipsilateral retina, and no contralateral RGC axons were observed in the dLGN (Figure 5D, right two columns).

We further examined whether retinocollicular topographic connectivity was established properly in the *Vax1*$^{AA/AA}$ mouse SC, which lacks contralateral RGC axon terminals (Figure 5C, bottom row). Axons from RGCs in the temporal retina are known to connect to the anterior SC, whereas those from the nasal retina link to the posterior SC (Lemke and Reber, 2005). In the perpendicular axis, RGC axons from the dorsal retina arrive at the lateral SC, and those from the ventral retina are wired to the medial SC. Thus, axons of Pax6 α-Cre-affected RGCs in the ventral and peripheral retina, which express membrane-localized EGFP (EGFP*) in *ROSA26* gene locus of *R26*^{tm4} Cre reporter mice

(Marquardt et al., 2001; Muzumdar et al., 2007), map to medial and peripheral parts of the SC of P30 *Vax1*$^{+/+}$ mice (Figure 5E, middle row). This pattern was also observed in the SCs of *Vax1*$^{AA/AA}$ littermate mice (Figure 5E, bottom row), implying that the retinocollicular topography is established properly in *Vax1*$^{AA/AA}$ mice.

Light-stimulated retinal and cortical responses in Vax1$^{AA/AA}$ mice

Next, we examined whether visual information can be properly processed in the retina and delivered to the brain in *Vax1*$^{AA/AA}$ mice. First, we tested the activities of P45 mouse retinas using electroretinography (ERG) recordings. The shapes of scotopic ERG a-waves, which reflect the function of rod photoreceptors, appeared normal in *Vax1*$^{AA/AA}$ mice, although the amplitudes of scotopic ERG b-waves, which are generated by bipolar cells and Müller glia in the inner retina downstream of photoreceptors (Miura et al., 2009), were decreased (Figure 6A [right column] and 6B). However, the amplitudes of photopic ERG a-waves, which reflect the activity of cone photoreceptors, were significantly decreased in *Vax1*$^{AA/AA}$ mice compared with *Vax1*$^{+/+}$ littermate mice (Figure 6A [left column] and 6C [graph in left]), leading to a consequent decrease in amplitudes of photopic ERG b-waves (Figure 6A [left column] and 6C [graph in right]). The reduced ERG waves in *Vax1*$^{AA/AA}$ mice might be related to the decrease in S-opsin–positive cone photoreceptors in the ventral retina (Figure S2C), a feature reminiscent of mouse retina deficient for the related *Vax2* gene (Alfano et al., 2011). However, we found no significant differences in other cell types in the retina and optic nerves in *Vax1*$^{AA/AA}$ mice compared with *Vax1*$^{+/+}$ littermates (Figure S2).

We also examined whether visual information received by the retina is delivered to the cortex via the dLGN in *Vax1*$^{AA/AA}$ mice. To this end, we recorded electrical activities of neurons in the monocular zone of the primary visual cortices (V1) in both hemispheres of mouse brain while giving the visual stimuli only to the left eye. We found that it predominantly triggered responses of cortical neurons in the right V1 of *Vax1*$^{+/+}$ mice;

conversely, it mainly activated neurons in the left V1 of *Vax1*$^{AA/AA}$ mice (Figure 6D and 6E). Collectively, these results demonstrate that *Vax1*$^{AA/AA}$ mouse retina senses a light stimulus and send visual information to the ipsilateral dLGN for subsequent delivery of the information to the visual cortex, whereas the information is sent to mainly to the contralateral brain areas in *Vax1*$^{+/+}$ mice.

Reduced visual acuity of Vax1*$^{AA/AA}$ *mice

We next examined whether the ipsilaterally-biased retinogeniculate and retinocollicular pathways influenced the visual responses of *Vax1*$^{AA/AA}$ mice. First, we tested whether the mice could discriminate light and dark spaces. We found that P45 *Vax1*$^{+/+}$ and *Vax1*$^{AA/AA}$ littermate mice generally spent longer periods in the dark chamber than in the illuminated chamber (Figure 6F; Movie S1 and S2). On the contrary, P45 retinal dystrophy 1 (*rd1*) mutant *C3H/HeJ* blind mice, which have a homozygous mutation of *phosphodiesterase 6b* (*Pde6b; Pde6b*$^{rd1/rd1}$*)* gene (Chang et al., 2002), spent equivalent periods in dark and light chambers (Figure 6F; Movie S3). These results suggest that *Vax1*$^{AA/AA}$ mice discriminate light and dark space as efficiently as *Vax1*$^{+/+}$ mice.

Second, we examined whether mice could recognize images that mimic a looming shadow of predator (Yilmaz and Meister, 2013). P45 mice were placed in a transparent box covered by a computer monitor displaying a black circle that expands by a 20° angle from the mouse head. *Vax1*$^{+/+}$ mice froze or hid under a shelter while the circle in the monitor expanded (Figure 6G; Movie S4). *Vax1*$^{AA/AA}$ mice also exhibited hiding and/or freezing responses; however, their response frequency was significantly lower than that of *Vax1*$^{+/+}$ mice (Figure 6G; Movie S5). *Pde6b*$^{rd1/rd1}$ mice showed no behavioral responses at all (Figure 3D; Movie S6). These results suggest that *Vax1*$^{AA/AA}$ mice could recognize the shadow pattern, but did so less efficiently than *Vax1*$^{+/+}$ mice.

Third, we investigated whether mice could discriminate near and far objects by placing them on a transparent plate, half of which was printed with a flannel pattern image (i.e., safe zone) and the other unprinted half extended over a floor with the same flannel pattern (i.e., cliff zone) (Sloane et al., 1978). P45 *Vax1*$^{+/+}$ mice stayed in the safe zone and rarely ventured into the cliff zone (Figure 6H; Movie S7). However, *Vax1*$^{AA/AA}$ littermate mice moved freely between cliff and safe zones (Figure 6H; Movie S8), as did P45 *Pde6b*$^{rd1/rd1}$ blind mice (Figure 6H; Movie S9). These results suggest that *Vax1*$^{AA/AA}$ mice have impaired depth perception, a visual capacity that requires bilateral RGC axon projections to ipsilateral and contralateral LGNs (Larsson, 2013; Petros et al., 2008).

Last, we assessed the visual acuity of mice by measuring optomotor responses (OMRs) to horizontally moving black and white vertical strips using OptoMotry (Prusky et al., 2004). P45 *Vax1*$^{+/+}$ mice turned their heads in the direction of vertical stripe movement (Figure 6I; Movie S10); however, P45 *Vax1*$^{AA/AA}$ and *Pde6b*$^{rd1/rd1}$ mice failed to show a valid OMR (Figure 6I; Movie S11 and S12). These results suggest that the visual acuity of *Vax1*$^{AA/AA}$ mice is significantly compromised compared with that of *Vax1*$^{+/+}$ mice.

Vax1$^{AA/AA}$ ***mice exhibit inverse oculomotor responses***

The OMR-based visual acuity test counts head-turn events to moving objects. Therefore, despite having normal visual perception, mice may not respond properly if their oculomotor system is abnormal. Interestingly, *Vax1*$^{AA/AA}$ mice startled in response to the stimuli, but did not show corresponding head-turn behavior (Figure 6I; Movie S8). This contrasted with *Pde6b*$^{rd1/rd1}$ blind mice, which showed no stimulus-dependent responses (Figure 6I; Movie S9). These results suggest that the reduced visual acuity of *Vax1*$^{AA/AA}$ mice might have resulted from an abnormal oculomotor system that cannot trigger proper head-turn responses.

Achiasmatic humans and dogs were also previously reported to have reduced visual acuity (Apkarian et al., 1995; Dell'Osso and Williams, 1995; Williams et al., 1994). Interestingly, they commonly exhibited seesaw nystagmus—an out of phase vertical oscillation in the two eyes in the absence of a visual stimulus. We thus tracked eye movements in P45 *Vax1*$^{+/+}$ and *Vax1*$^{AA/AA}$ littermate mice, and found the eyes of *Vax1*$^{AA/AA}$ mice oscillated in an oval track in the absence of visual stimulus (Figure 7A and 7B; Movie S11). The oscillatory cycles of the two eyes were out of phase in the vertical axis but in phase in the horizontal axis (Figure 7A, right column; Movie S11), phenocopying the seesaw nystagmus of achiasmatic humans and dogs. In contrast, the eyes of *Vax1*$^{+/+}$ littermate mice gazed stably (Figure 7A, left column; Movie S10).

Spontaneous oscillations of *Vax1*$^{AA/AA}$ mouse eyes were also evident during pupil contraction responses to light illumination (Movie S13). However, the speed of pupil contraction was not significantly different between *Vax1*$^{+/+}$ and *Vax1*$^{AA/AA}$ mice (Figure 7C and 7D; Movie S12 and S13). We also examined pupil contraction after illuminating only one eye with light. Monocular illumination to *Vax1*$^{+/+}$ mice induced immediate contraction of pupils in direct (i.e., stimulated) eyes, followed by contraction of the pupils of consensual (i.e., unstimulated) eyes (Figure 7E and 7F; Movie S14). Interestingly, pupil contraction occurred faster in the consensual eyes of *Vax1*$^{AA/AA}$ mice (Figure 7C; Movie S15), suggesting that pupillary oculomotor outputs are sent in opposite routes in *Vax1*$^{AA/AA}$ mice compared with *Vax1*$^{+/+}$ mice.

We also investigated the optokinetic reflex (OKR) of mouse eyes to moving objects (Cahill and Nathans, 2008). *Vax1*$^{+/+}$ mice rotate their eyes correspondingly and periodically in the direction of movement of black and white vertical stripes, which rotate clockwise or counter clockwise (Figure 7G and 7H; Movie S16 and S18); however, they did not rotate their eyes when the stripes converged, diverged, or stopped in the front eye field (Figure 7G and 7H; Movie S20, S22, and S24). Interestingly, the eyes of *Vax1*$^{AA/AA}$ mice, which oscillated constitutively in the absence of visual stimulation, stopped moving when the stripes moved clockwise or counterclockwise (Figure 7G and 7H; Movie S17 and S19).

These results suggest that *Vax1*$^{AA/AA}$ mice recognize the movement of objects; however, their oculomotor systems do not operate in the same way as they do in *Vax1*$^{+/+}$ mice, which rotate their eyes and heads correspondingly to moving objects.

DISCUSSION

Many vertebrate organs exhibit bilateral symmetry. However, these paired organs are not simply duplications, but instead are frequently functional complements of each other. For instance, the left hemisphere of the human cerebral cortex houses the language center, whereas the right hemisphere is where pattern recognition occurs (Wolman, 2012). This is demonstrated by the ‘split-brain’ phenomenon, in which an individual whose two cerebral hemispheres are not connected by the CC cannot match words to the corresponding objects. In vertebrate binocular visual systems, bilateral projection of RGC axons at the OC is necessary for the brain to receive visual information coming from the two eyes (Herrera et al., 2019; Petros et al., 2008). Therefore, proper development of the OC is required for stereoscopic vision—achieved by overlapping focal-drifted images from each eye—and the coordination of bilateral oculomotor responses.

Agenesis of the OC (AOC) has been reported in various vertebrates, including humans, dogs, and fish (Apkarian et al., 1995; Dell'Osso and Williams, 1995; Karlstrom et al., 1996; Williams et al., 1994). However, the molecular features of AOC have not been identified except in *belladonna* (*bel*) zebrafishes, which carry mutations in the LIM homeobox 2 (*lhx2*) gene (Seth et al., 2006). In the achiasmatic *bel* mutants, ventral diencephalic regions, including the preoptic area (POA), vHT and OS, are not patterned properly by virtue of the failure to express key genes, including *vax2*, *zic2.1*, and *pax2.1* (Seth et al., 2006). However, Lhx2 and Pax2 are properly expressed in the *Vax1*$^{AA/AA}$ mouse OS (Figure 2C; Lhx2 data not shown). Vax2 and Zic2 are not present in the OS of

Vax1$^{+/+}$ and *Vax1*$^{AA/AA}$ mice, but are expressed in the ventral and ventral-temporal retina, respectively (Figure 3D; Vax2 data not shown). Furthermore, the OS was specified properly in *Vax1*$^{AA/AA}$ mice, without the expression of the retinal markers, Pax6 and Vsx2 (Figure 2C and 2D). The vHT was also correctly specified in *Vax1*$^{AA/AA}$ mice through appropriate expression of Shh (Figure 3C). Therefore, it is unlikely that AOC in *Vax1*$^{AA/AA}$ mice results from the failure to specify the OS and vHT.

Despite normal specification, OS maturation was delayed in *Vax1*$^{AA/AA}$ mice. In these mice, the optic fissures at the OS were closed completely by E16.5, whereas in *Vax1*$^{+/+}$ mice, they had already disappeared by E14.5 and OS cells had spread among RGC axons in a salt-and-pepper pattern (Figure 2C and 2D). The morphology of the E14.5 *Vax1*$^{AA/AA}$ mouse OS was largely similar to that of E12.5 *Vax1*$^{+/+}$ mice, whose OS cells still exhibited neuroepithelial characteristics (Figure 2B). The molecular mechanisms underlying the maturation of OS cells still remain largely unknown, although several markers of OS cell lineage have been identified. For instance, Nestin and Ecad are expressed in the OS neuroepithelium; S100ß is expressed in OS APCs; and glial fibrillary acidic protein (Gfap) is expressed in OS astrocytes (Tao and Zhang, 2014). These markers, however, are not mutually exclusive. S100ß can be detected together with Ecad in OS cells (Figure 2D), suggesting an OS cell transition state between neuroepithelium and APC. As a result, it is difficult to dissect developmental stages of OS cells clearly with the limited information available. Thus, a more comprehensive understanding of OS maturation will require the identification of additional markers that are selectively expressed at specific OS developmental stages.

It has been proposed that Vax1 specifies the OS in vertebrates by directly suppressing the expression of a retinal fate determinant Pax6 (Bertuzzi et al., 1999; Mui et al., 2005). Expression of Pax6 in the OS was suppressed properly in *Vax1*$^{AA/AA}$ mice, whereas it was induced ectopically in the *Vax1*$^{-/-}$ mouse OS (Figure 2C). The ability of Vax1^{AA} to bind DNA sequences of *Pax6* α*-enhancer* were not different from that of Vax1 (Figure 4B), suggesting that Vax1^{AA} could regulate target gene expression as efficiently as

Vax1. Therefore, Vax1 transcription factor activity might not be crucial for OS maturation, which was delayed in *Vax1*$^{AA/AA}$ mice, although it might be necessary for the expression of other target genes, including gonadotrophin-releasing hormone (GnRH) in the SCN and POA (data not shown).

Achiasmatic animals, including the *Vax1*$^{AA/AA}$ mice reported here, exhibit a seesaw nystagmus characterized by failure to maintain gaze with the eyes at vertical axis (Apkarian et al., 1995; Dell'Osso et al., 1998). The rostral interstitial nucleus of medial longitudinal fasciculus (riMLF) and the interstitial nucleus of Cajal (INC) in the tegmentum of the midbrain has been identified as a key regulatory center for vertical gaze (Buuttner et al., 2002; Zee, 1986). riMLF neurons project directly to the oculomotor nucleus (ON) in the midbrain, and indirectly via the INC, to trigger ocular muscle contraction (Buuttner et al., 2002). Medial riMLF neurons innervate the third cranial nerve (CN-III; also called the ocular motor nerve) in the ON to stimulate the ipsilateral inferior rectum (IR) muscle, which is responsible for downward eye rotation. They are also wired to the fourth cranial nerve (CN-IV; also called the trochlear nerve) across the PC to stimulate the contralateral superior oblique (SO) muscle, which mediates nasal-downward eye rotation. Efferent projections forming the lateral riMLF reach CN-III to regulate contractions of the ipsilateral inferior oblique (IO) muscle and the contralateral superior rectus (SR) muscle, which mediate temporal-upward and upward rotations, respectively.

RGC axons innervate brain areas bilaterally in *Vax1*$^{+/+}$ mice (Figure 5C – 5E). Therefore, SC and riMLF neurons at both sides can be activated even by monocular stimulation, consequently the four ocular muscles—IR, SO, IO and SR—can contract simultaneously to result in vertical gaze. In contrast, the SC receives visual inputs only from ipsilateral eyes in *Vax1*$^{AA/AA}$ mice (Figure 5C). Therefore, signals from the right eye in *Vax1*$^{AA/AA}$ mice might induce contractions of IR and IO in the right eye and SR and SO in the left eye, resulting in nasal-downward pendular motion of the right eye and temporal-upward pendular movement of the left eye (Figure 7A; Figure S3). This vertically out of phase but horizontally in-phase eye movement is then followed by temporal-upward and

nasal-downward pendular motions, completing one oscillation cycle. This alternating eye movement, therefore, suggests that the signals from the two eyes are desynchronized and/or feeding back on each other.

SC neurons are also connected to the paramedian pontine reticular formation (PPRF), a horizontal gaze center in the pons that also receives oculomotor inputs from ipsilateral prefrontal cortex (Buttner-Ennever and Buttner, 1988; Zee, 1986). The PPRF receives inputs mainly from the contralateral SC and delivers them to the neighboring abducens nucleus (ABN). Abducens internuclear neurons (AIN) in the ABN then relay the signals to CN-III across the midline to stimulate the medial rectus (MR) ocular muscle, while abducens motor neurons (AMN) in the ABN connect ipsilaterally to the lateral rectus (LR). Given the binocular nature of efferent nerve fibers of ABN neurons, contractions of the MR in one eye and the LR in the other eye rotate both eyes in the same direction (Figure 7C). Horizontal gaze is therefore achieved when MR and LR in the same eye are activated simultaneously. However, because of the seesaw nystagmus, horizontal eye gaze was not observed in *Vax1*$^{AA/AA}$ mice.

Vax1$^{AA/AA}$ mouse eyes also failed to pursue moving objects (Figure 7G). However, instead of rotating correspondingly in the direction of object movement as *Vax1*$^{+/+}$ mice, the eyes of *Vax1*$^{AA/AA}$ mice frequently stopped oscillating when mice were presented objects moving clockwise or counterclockwise (Figure 7G; Movie S17 and S19). This stimulus-driven ectopic gaze of *Vax1*$^{AA/AA}$ mouse eyes might result from the combinatorial activation of extraocular muscles. As discussed above, the seesaw nystagmus of *Vax1*$^{AA/AA}$ mice is likely driven by alternating activation IR+IO and SR+SO ocular muscles. Therefore, IR+IO-driven nasal (and downward) movement of the right eye could be antagonized by LR-induced temporal movement in response to clockwise movement of the object. At the same time, SR+SO-driven temporal (and upward) movement of the left eye might be antagonized by MR-induced nasal movement. However, given the presence of the respective downward and upward forces after antagonism by the LR and MR, the right

eye position is slightly below the center and the left eye position is slightly above the center during the ectopic gaze in responding to clockwise stripe rotation (Figure 7G).

The *bel rev* achiasmatic zebrafish model also exhibits nystagmus when facing non-moving stripes (Huang et al., 2006). However, the nystagmus disappears in the dark and after non-patterned illumination of the visual field, which trigger seesaw nystagmus in achiasmatic mammals (Apkarian et al., 1995; Dell'Osso et al., 1998) (Figure 7A). Furthermore, in contrast to the stimulus-driven ectopic gaze in achiasmic *Vax1*$^{AA/AA}$ mice (Figure 7G), *bel rev* zebrafish exhibit reversed horizontal OKR in response to the rotation of stripes (Neuhauss et al., 1999; Rick et al., 2000). It was proposed that the ipsilateral RGC projection supplies a reversed retinal slip velocity input to the optokinetic system in zebrafish to elicit eye movements that compensate for retinal slip in the wrong direction (Neuhauss et al., 1999; Rick et al., 2000). However, reversed OKR and postural abnormalities have not been reported in humans (Apkarian et al., 1995), dogs (Dell'Osso and Williams, 1995; Hogan and Williams, 1995), or mice (Figure 7G). Therefore, the oculomotor circuits in animals with a non-stereoscopic visual system (like zebrafish) is likely different from those in the stereoscopic visual systems of mammals.

The oculomotor circuit also controls bilateral pupillary contraction, which is triggered by RGCs that are wired to the pretectal nucleus (PN) in the midbrain (Szabadi, 2018). PN neurons relay these signals to the Edinger-Westphal nucleus (EWN), which projects axons to the ipsilateral CN-III to induce pupillary contraction (Hultborn et al., 1978; Kourouyan and Horton, 1997). It has been suggested that the EWN receives signals from ipsilateral and contralateral PNs to induce bilateral pupillary contraction. However, given the faster pupil contraction of directly stimulated eyes compared with consensual eyes in *Vax1*$^{+/+}$ mice (Figure 7E), the PN might primarily stimulate the contralateral EWN in mice. Consequently, the repeated midline crossings at retina-PN and PN-EWN axes enable the directly stimulated eye to respond faster than the consensual eye. However, an ipsilateral retina-PN connection followed by a contralateral PN-EWN connection might result in an inverse order of pupillary contraction in *Vax1*$^{AA/AA}$ mice (Figure 7E). These results suggest

that the operation of the oculomotor system depends on a constant number of midline crossings; therefore, the system cannot function properly if one of those commissures is missing.

The axons of SC neurons also project contralaterally to the cervical spinal cord through the tectospinal tract, and can trigger head turns in response to visual stimuli (Gandhi and Katnani, 2011). Therefore, activation of the right SC, which receives a majority of its inputs from the left eye, which captures objects in the left visual field, predominantly contracts the left neck muscle to trigger a leftward head turn in *Vax1*$^{+/+}$ mice. Given the exclusive ipsilateral retinocollicular connection, the spinal outputs in achiasmatic *Vax1*$^{AA/AA}$ mice are likely inverse to those in *Vax1*$^{+/+}$ mice. This might make *Vax1*$^{AA/AA}$ mice turn their heads in the direction opposite the stimulus. *Vax1*$^{AA/AA}$ mice, however, startled instead of turning their heads in the direction opposite the movement of horizontally drifting stripes (Figure 6G). These results suggest that head-turn behavior is not only determined by eye-SC-spinal cord circuits, but is also affected by cortical circuits that regulate activity of the PPRF to pursue the objects (Gandhi and Katnani, 2011).

METHODS

Mouse strains

Vax1$^{-/-}$ and *Pax6* α*-Cre* mice were reported previously (Bertuzzi et al., 1999; Marquardt et al., 2001). *Gt(ROSA)26Sor*$^{tm4(ACTB\text{-}tdTomato,\text{-}EGFP)Luo}$*/J* (*R26*^{tm4}) and *Gt(ROSA)26Sor*$^{tm11(CAG\text{-}tdTomato*,\text{-}GFP*)Nat}$*/J* (*R26*^{tm11}) mouse strains were purchased from Jackson laboratory (Muzumdar et al., 2007; Wang et al., 2019).

Vax1$^{AA/AA}$ mice were generated using CRISPR/Cas9 system with a CRISPR RNA (crRNA) and a trans-activating crRNA (tracrRNA) in following procedures. Two crRNAs were designed to target two nearby sites of the second exon of *Vax1* gene, which include DNA sequences encoding K101 and R102 (Figure S1A). The sequences of crRNAs were: #1, 5-TGGATCTGGACCGGCCCAAG-3 and #2, 5-AAGGACGTGCGAGTCCTCTT-3. The synthetic single-stranded DNA oligonucleotide (ssODN) containing missense (KR-to-AA) and synonymous mutations, 5'-TCTCAGAGAGATTGAGCTGCCGAGCCAGCTCGGTTCTCTCCCGGCCCACCACGTATTGGCAACGCTGGAACTCCATCTCCAGCCTGTAGAGCTGCTCAGCTGTAAACGAGGTCCTGGTCGCCGCGGGCCGGTCCAGATCCAAGCCTTTGGGCAGGATGATTTCTCGGATAGACCCCTTGGCATCTAGGAAAGGG-3' (IDT, Inc., USA), was used as a donor DNA. We then injected those crRNA/tracrRNA duplex and ssODN together with Cas9 mRNA (Toolgen, Inc., Seoul, Korea) into the cytoplasm of one cell-stage *C57BL/6J* mouse embryos. To screen the founders carrying the KR-to-AA mutation in the *Vax1* gene, PCR was performed (Figure S1B). The primer sequences to identify the KR-to-AA knock-in allele were: 5'-AGTATGAAGTTAGCCCCCTTGG-3' as a forward primer and 5'-GTAAACGAGGTCCTGGTCGC-3' as a knock-in-specific reverse primer, and those for wild-type allele, 5'-AAGAGGACTCGCACGTCC-3' as a wild-type-specific forward primer and 5'-AGGAAAGGCAAGCTGTCATC-3' as a reverse primer. Then, the genomic regions spanning the mutated second exon of the founder mice were validated by direct-sequencing analysis (Bionics Co., Ltd., Seoul, Korea). We obtained three *Vax1*$^{+/AA}$ male mice after analyzing 83 pubs obtained from the 439 injected embryos. The off-springs of

the *Vax1*$^{+/AA}$ mouse were then backcrossed with wild-type *C57BL/6J* mice over 6 generations to eliminate unwanted off-target mutations introduced by CRISPR/Cas9. All experiments were performed according to the Korean Ministry of Food and Drug Safety (MFDS) guidelines for animal research. The protocols were certified by the Institutional Animal Care and Use Committee (IACUC) of KAIST (KA2010-17) and Yonsei University (A-201507-390-01). All mice used in this study were maintained in a specific pathogen-free facility of KAIST Laboratory Animal Resource Center and Yonsei Laboratory Animal Research Center.

Cell and explants culture

Human cervical cancer HeLa cells and human embryonic kidney (HEK) 293T cells were cultured in Dullbeco's Eagle Modified Media (DMEM) supplemented with 10% fetal bovine serum (FBS). For the luciferase assay, HEK293T cells (10^5) were transfected with 1 μg pCAGIG-V5 vectors encode Vax1, Vax1^{AA}, or Vax1(R152S) cDNA together with pGL3-Tcf7l2-luciferase (0.2 μg) and pCMV-β-gal (0.2 μg) reporter constructs. Luciferase activities in the transfected cells were measured at 24h post-transfection, and normalized by β-galactosidase activities to obtain relative luciferase activity of the cells. To test cellular penetration of Vax1 protein, V5 peptides or V5-Vax1 proteins, which were purified from HEK293T cells, were added into the growth media (1.5 pmol/ml [final concentration]) of HeLa cells, which express GFP-Sdc2. Distribution of V5 peptides and V5-Vax1 proteins on cell surface and inside the cells were examined by immunostaining with mouse anti-V5 and chicken anti-GFP antibodies.

Retinal explants prepared as described previously (Kim et al., 2014). Briefly, the retina was prepared from mouse embryos at E13, and mixed with collagen in DMEM with 10% FBS. The retinal explants in collagen were then cultured in Neurobasal medium containing B27 supplement (Invitrogen Inc.) for 48h to allow the axons grow from the explants. 6X-Histidine peptides or Vax1-6X-His proteins, which were purified from E.coli, were then added into the culture medium (2 pmol/ml [final concentration]) of retinal

explants. Alternatively, the retinal explants were placed next to collagen droplets containing HEK293 cells (10^5 cells/droplet), which express Vax1 or Vax1^{AA}. The lengths of retinal axons grown from the explants were measured before and after the treatments to determine axon growth rate.

Slab embryo culture with collagen gel was also performed as described previously (Kim et al., 2014). Collagen droplets mixed with Flag peptides (10 μg/ml) or Flag-Vax1 proteins (200 μg/ml) were prepared and placed into the third ventricle of the slab embryos. The embryos were then incubated for 12 hr at 37°C in a humidified atmosphere supplemented with 7% CO_2.

Detection of Vax1 proteins in the growth medium

Heparin (10 mg/ml) was added into growth medium of HEK293T cells (10^7) express V5-Vax1 or V5-Vax1^{AA}. Macromolecules including the proteins and lipids in the growth medium were precipitated by adding trichloroacetic acid (TCA; 20% final). The precipitates were washed with cold acetone three times and dissolved in 2X-SDS sample buffer for SDS-PAGE followed by WB to detect Vax1 proteins released in the growth medium.

Immunohistochemistry and in situ RNA hybridization

Distribution of proteins in HeLa and mouse embryonic cells were examined by immunostaining. Cultured cells were fixed in 4% paraformaldehyde (PFA) in phosphate buffered saline (PBS) for 10 mins at 36-h post-transfection. Sections of mouse embryos, eyes, and brain slabs were fixed in 4%PFA/PBS at room temperature for 2 h, and then put in a 20% sucrose/PBS solution at 4°C for 16 h before embedding in OCT (optimal cutting temperature) medium for cryofreezing and cryosection.

The cells and sections were incubated in a blocking solution containing 0.2% Triton X-100, 5% normal donkey serum, and 2% bovine serum albumen (BSA) in PBS for 1 h. To stain the proteins in the cells, the samples were incubated with the indicated primary

antibodies in blocking solution without 0.2% Triton X-100 at 4°C for 16 h and then with the appropriate secondary antibodies conjugated with fluorophores. Immunofluorescence was subsequently analyzed using Olympus FV1000 and Zeiss LSM810 confocal microscopes. Antibody information is provided in Table S1.

Distributions of mRNA of interest in the embryonic sections were detected by *in situ* hybridization (ISH) with dioxygenin (DIG)-labeled RNA probes and visualized them by immunostaining with alkaline phosphatase (AP)-conjugated α-DIG followed by AP-mediated colorization, as it was described in a previous report (Kim et al., 2014).

Chromatin immunoprecipitation (ChIP) and PCR

Chromatin immunoprecipitation was done as it was described previously (Mui et al., 2005). E10.5 mouse embryonic heads were isolated and chopped into small pieces in prior to the incubation in 1% formaldehyde in PBS at room temperature for 10 min. The nuclei were isolated for the immunoprecipitation with rabbit anti-Vax1 antibody or pre-immune rabbit IgG. DNA fragments coprecipitated with the antibodies were purified by phenol/chloroform/isoamyl alcohol extraction, and 100 ng of these immunoprecipitated DNAs were used as templates for PCR amplification of the Pax6 α-enhancer.

Electroretinogram (ERG)

Mice were either dark- or light-adapted for 12 h before ERG recording and anesthetized with 2,2,2-tribromoethanol (Sigma). After the pupils of the mice were dilated by 0.5% tropicamide, a gold-plated objective lens was placed on the cornea and silver-embedded needle electrodes were placed at the forehead and tail. The ERG recordings were performed using Micron IV retinal imaging microscope (Phoenix Research Labs) and analyzed by Labscribe ERG software according to the manufacturer's instruction. To obtain scotopic ERG a- and b-waves, a digital bandpass filter ranging from 0.3 to 1,000 Hz

and stimulus ranging from −2.2 to 2.2 log(cd·s m^{-2}) were used. To yield photopic ERG a- and b-waves, filter ranging from 2 to 200 Hz and stimulus ranging from 0.4 to 2.2 log(cd·s m^{-2}) with 1.3 log(cd·s m^{-2}) background were used.

In vivo extracellular recording and data analysis

We performed *in vivo* extracellular recordings in the monocular V1 (bregma, -3.50 mm; lateral, 2.50 mm; depth, 0.70 mm) of $Vax1^{+/+}$ and $Vax1^{AA/AA}$ mice. Mice were anesthetized with the urethane (2 g per kg body weight, intraperitoneal injection) and restrained in a custom-designed head-fixed apparatus. A small craniotomy with the diameter of ~0.5 mm was made over V1 of the left and the right hemispheres, and we inserted a 32-channel silicon electrode (A1x32-Poly3-10mm-50-177-CM32, Neuronexus) using micro-drive motorized manipulator (Siskiyou). After waiting 20 ~ 30 minutes for stabilization, we started recording visual responses by presenting a full-field flashing light for 5 times to the left eye. The visual stimuli were presented at 10 Hz for 500ms, 5 pulses of 50 ms duration, and total 30 trials through a gamma-corrected monitor. Extracellular signals were filtered between 500~5000 Hz at 30 kHz sampling rate, amplified by miniature digital head-stage (CerePlex μ, Blackrock Microsystems), and saved through data acquisition system (CerePlex Direct, Blackrock Microsystems). We performed spike sorting using the Klusters software (http://neurosuite.sourceforge.net/) and further analyzed firing rates of isolated single units using MATLAB. We analyzed the z-score of firing activity in each single unit from -1 to +2 s of the onset of the visual stimuli and plotted peri-stimulus time histogram (PSTH) of the normalized activity. Firing rate change index (FR index) of individual cells was calculated using the following formula:

FR index = (mean z-score for 1 s after stimuli onset - mean z-score for 1 s before stimuli onset) / (mean z-score for 1 s after stimuli onset + mean z-score for 1 s before stimuli onset)

Light-dark chamber assay

The light-dark test apparatus was composed of light (21cm(width, W) X 29cm(depth, D) X 20cm(height, H), 700 lux) and dark (21cm(W) X 13cm(D) X 20cm(H), ~5 lux) chambers. The dark chamber is separated from light chamber by an entrance in the middle wall (5cm(W) X 8cm(H)). Mice were introduced in the light chamber with their heads toward the opposite side of the dark chamber and allowed to freely explore the apparatus for 10 min. Amounts of time spent in the light and dark chambers and number of transitions were analyzed by Ethovision XT10 software (Noldus).

Looming assay

Looming test was performed as described previously with some modifications (Yilmaz and Meister, 2013). Briefly, the behavioral arena was prepared with an open-top acryl box (30cm(W) X 30cm(D) X 30cm(H)), which contains a nest in the shape of a triangular prism (10cm(W) X 12cm(D) X 10cm(H)). The looming disk was programmed as a black circle in a gray background, increasing its size from 2 degrees of visual angle to 20 degrees in 250 ms and maintained for 250 ms. The pattern was repeatedly presented 10 times with 500 ms of interval for each trial.

Optomotor response (OMR)

Mouse visual acuity was measured with the OptoMotry system (Cerebral Mechanics) as previously described (Prusky et al., 2004). Mice were adapted to ambient light for 30 mins and then placed on the stimulus platform, which is surrounded by four computer monitors displaying black and white vertical stripe patterns. An event that mice stopped moving and began tracking the stripe movements with reflexive head-turn was counted as a successful visual detection. The detection thresholds were then obtained from the OptoMotry software.

Measurements of pupillary contraction and optokinetic response (OKR)

Mouse heads were mounted to a plate and clamped to a holder to prevent head movement during measurement. Images of a mouse eye that show the pupil and the corneal reflection were recorded by CCD camera (120/240 Hz) with Infrared (IR) filter (ISCAN Inc.). To measure the OKR, the head-fixed mice were put in front of the screens that display gray background or black and white vertical stripes (30% contrast) moving at a spatial frequency of 0.2 c/d and angular velocity of 12 d/s. To examine the pupil contraction, the mice were kept in the dark for 30 secs and then exposed to 500 lux of light for 10 secs. The pupil position and diameter were measured by the ISCAN software (ISCAN Inc.).

Statistical analyses

Statistical tests were performed using Prism Software (GraphPad; v5.0) measurement tools. All data from statistical analysis are presented as the average ± STD. Comparison between two groups was done by unpaired Student's t-test, and the differences among multiple groups were determined by analysis of variance (ANOVA) with Tukey's post-test used to determine the significant differences among multiple groups. P-values < 0.01 were considered as statistically significant results.

ACKNOWLEDGEMENTS

We thank to Ilsong Choi and Anna Shin for helping mouse ocular behavior tests. This work was supported by the National Research Foundation of Korea (NRF) grants (NRF-2017R1A2B3002862 and NRF-2018R1A5A1024261) funded by Korean Ministry of Science and ICT (MSIT), South Korea. This study was performed in strict accordance with the recommendations in the Guide for the Care and Use of Laboratory Animals of the

Korean Ministry of Agriculture, Food, and Rural Affairs. All of the animals were handled according to approved institutional animal care and use committee (IACUC) protocols (#13-130) of Korea Advanced Institute of Science and Technology.

REFERENCES

Alfano, G., Conte, I., Caramico, T., Avellino, R., Arno, B., Pizzo, M.T., Tanimoto, N., Beck, S.C., Huber, G., Dolle, P.*, et al.* (2011). Vax2 regulates retinoic acid distribution and cone opsin expression in the vertebrate eye. Development *138*, 261-271.

Apkarian, P., Bour, L.J., Barth, P.G., Wenniger-Prick, L., and Verbeeten, B., Jr. (1995). Non-decussating retinal-fugal fibre syndrome. An inborn achiasmatic malformation associated with visuotopic misrouting, visual evoked potential ipsilateral asymmetry and nystagmus. Brain *118*, 1195-1216.

Bertuzzi, S., Hindges, R., Mui, S.H., O'Leary, D.D., and Lemke, G. (1999). The homeodomain protein vax1 is required for axon guidance and major tract formation in the developing forebrain. Genes Dev *13*, 3092-3105.

Beurdeley, M., Spatazza, J., Lee, H.H., Sugiyama, S., Bernard, C., Di Nardo, A.A., Hensch, T.K., and Prochiantz, A. (2012). Otx2 binding to perineuronal nets persistently regulates plasticity in the mature visual cortex. J Neurosci *32*, 9429-9437.

Bharti, K., Gasper, M., Bertuzzi, S., and Arnheiter, H. (2011). Lack of the ventral anterior homeodomain transcription factor VAX1 leads to induction of a second pituitary. Development *138*, 873-878.

Buttner-Ennever, J.A., and Buttner, U. (1988). Neuroanatomy of the oculomotor system. The reticular formation. Rev Oculomot Res *2*, 119-176.

Buuttner, U., Buuttner-Ennever, J.A., Rambold, H., and Helmchen, C. (2002). The contribution of midbrain circuits in the control of gaze. Ann N Y Acad Sci *956*, 99-110.

Cahill, H., and Nathans, J. (2008). The optokinetic reflex as a tool for quantitative analyses of nervous system function in mice: application to genetic and drug-induced variation. PLoS One *3*, e2055.

Cardin, A.D., and Weintraub, H.J. (1989). Molecular modeling of protein-glycosaminoglycan interactions. Arteriosclerosis *9*, 21-32.

Chang, B., Hawes, N.L., Hurd, R.E., Davisson, M.T., Nusinowitz, S., and Heckenlively, J.R. (2002). Retinal degeneration mutants in the mouse. Vision Res *42*, 517-525.

Chiang, C., Litingtung, Y., Lee, E., Young, K.E., Corden, J.L., Westphal, H., and Beachy, P.A. (1996). Cyclopia and defective axial patterning in mice lacking Sonic hedgehog gene function. Nature *383*, 407-413.

Dell'Osso, L.F., and Williams, R.W. (1995). Ocular motor abnormalities in achiasmatic mutant Belgian sheepdogs: unyoked eye movements in a mammal. Vision Res *35*, 109-116.

Dell'Osso, L.F., Williams, R.W., Jacobs, J.B., and Erchul, D.M. (1998). The congenital and see-saw nystagmus in the prototypical achiasma of canines: comparison to the human achiasmatic prototype. Vision Res *38*, 1629-1641.

Erskine, L., Reijntjes, S., Pratt, T., Denti, L., Schwarz, Q., Vieira, J.M., Alakakone, B., Shewan, D., and Ruhrberg, C. (2011). VEGF signaling through neuropilin 1 guides commissural axon crossing at the optic chiasm. Neuron *70*, 951-965.

Gandhi, N.J., and Katnani, H.A. (2011). Motor functions of the superior colliculus. Annu Rev Neurosci *34*, 205-231.

Guido, W. (2018). Development, form, and function of the mouse visual thalamus. J Neurophysiol *120*, 211-225.

Hallonet, M., Hollemann, T., Pieler, T., and Gruss, P. (1999). Vax1, a novel homeobox-containing gene, directs development of the basal forebrain and visual system. Genes Dev *13*, 3106-3114.

Herrera, E., Brown, L., Aruga, J., Rachel, R.A., Dolen, G., Mikoshiba, K., Brown, S., and Mason, C.A. (2003). Zic2 patterns binocular vision by specifying the uncrossed retinal projection. Cell *114*, 545-557.

Herrera, E., Erskine, L., and Morenilla-Palao, C. (2019). Guidance of retinal axons in mammals. Semin Cell Dev Biol *85*, 48-59.

Hogan, D., and Williams, R.W. (1995). Analysis of the retinas and optic nerves of achiasmatic Belgian sheepdogs. The Journal of comparative neurology *352*, 367-380.

Huang, Y.Y., Rinner, O., Hedinger, P., Liu, S.C., and Neuhauss, S.C. (2006). Oculomotor instabilities in zebrafish mutant belladonna: a behavioral model for congenital nystagmus caused by axonal misrouting. J Neurosci *26*, 9873-9880.

Huberman, A.D., Feller, M.B., and Chapman, B. (2008). Mechanisms underlying development of visual maps and receptive fields. Annu Rev Neurosci *31*, 479-509.

Hultborn, H., Mori, K., and Tsukahara, N. (1978). The neuronal pathway subserving the pupillary light reflex. Brain Res *159*, 255-267.

Karlstrom, R.O., Trowe, T., Klostermann, S., Baier, H., Brand, M., Crawford, A.D., Grunewald, B., Haffter, P., Hoffmann, H., Meyer, S.U.*, et al.* (1996). Zebrafish mutations affecting retinotectal axon pathfinding. Development *123*, 427-438.

Kim, J.W., and Lemke, G. (2006). Hedgehog-regulated localization of Vax2 controls eye development. Genes Dev *20*, 2833-2847.

Kim, N., Min, K.W., Kang, K.H., Lee, E.J., Kim, H.T., Moon, K., Choi, J., Le, D., Lee, S.H., and Kim, J.W. (2014). Regulation of retinal axon growth by secreted Vax1 homeodomain protein. eLife, e02671.

Kourouyan, H.D., and Horton, J.C. (1997). Transneuronal retinal input to the primate Edinger-Westphal nucleus. J Comp Neurol *381*, 68-80.

Kuwajima, T., Yoshida, Y., Takegahara, N., Petros, T.J., Kumanogoh, A., Jessell, T.M., Sakurai, T., and Mason, C. (2012). Optic chiasm presentation of Semaphorin6D in the context of Plexin-A1 and Nr-CAM promotes retinal axon midline crossing. Neuron *74*, 676-690.

Larsson, M. (2013). The optic chiasm: a turning point in the evolution of eye/hand coordination. Front Zool *10*, 41.

Lee, E.J., Kim, N., Park, J.W., Kang, K.H., Kim, W.I., Sim, N.S., Jeong, C.S., Blackshaw, S., Vidal, M., Huh, S.O.*, et al.* (2019). Global Analysis of Intercellular Homeodomain Protein Transfer. Cell Rep *28*, 712-722 e713.

Lemke, G., and Reber, M. (2005). Retinotectal mapping: new insights from molecular genetics. Annu Rev Cell Dev Biol *21*, 551-580.

Luppi, P.H., Fort, P., and Jouvet, M. (1990). Iontophoretic application of unconjugated cholera toxin B subunit (CTb) combined with immunohistochemistry of neurochemical substances: a method for transmitter identification of retrogradely labeled neurons. Brain Res *534*, 209-224.

Marquardt, T., Ashery-Padan, R., Andrejewski, N., Scardigli, R., Guillemot, F., and Gruss, P. (2001). Pax6 is required for the multipotent state of retinal progenitor cells. Cell *105*, 43-55.

Miura, G., Wang, M.H., Ivers, K.M., and Frishman, L.J. (2009). Retinal pathway origins of the pattern ERG of the mouse. Exp Eye Res *89*, 49-62.

Miyata, S., Komatsu, Y., Yoshimura, Y., Taya, C., and Kitagawa, H. (2012). Persistent cortical plasticity by upregulation of chondroitin 6-sulfation. Nat Neurosci *15*, 414-422, S411-412.

Mui, S.H., Kim, J.W., Lemke, G., and Bertuzzi, S. (2005). Vax genes ventralize the embryonic eye. Genes Dev *19*, 1249-1259.

Muzumdar, M.D., Tasic, B., Miyamichi, K., Li, L., and Luo, L. (2007). A global double-fluorescent Cre reporter mouse. Genesis *45*, 593-605.

Neuhauss, S.C., Biehlmaier, O., Seeliger, M.W., Das, T., Kohler, K., Harris, W.A., and Baier, H. (1999). Genetic disorders of vision revealed by a behavioral screen of 400 essential loci in zebrafish. J Neurosci *19*, 8603-8615.

Peng, J., Fabre, P.J., Dolique, T., Swikert, S.M., Kermasson, L., Shimogori, T., and Charron, F. (2018). Sonic Hedgehog Is a Remotely Produced Cue that Controls Axon Guidance Trans-axonally at a Midline Choice Point. Neuron *97*, 326-340 e324.

Petros, T.J., Rebsam, A., and Mason, C.A. (2008). Retinal axon growth at the optic chiasm: to cross or not to cross. Annu Rev Neurosci *31*, 295-315.

Prusky, G.T., Alam, N.M., Beekman, S., and Douglas, R.M. (2004). Rapid quantification of adult and developing mouse spatial vision using a virtual optomotor system. Invest Ophthalmol Vis Sci *45*, 4611-4616.

Rice, D.S., Williams, R.W., and Goldowitz, D. (1995). Genetic control of retinal projections in inbred strains of albino mice. J Comp Neurol *354*, 459-469.

Rick, J.M., Horschke, I., and Neuhauss, S.C. (2000). Optokinetic behavior is reversed in achiasmatic mutant zebrafish larvae. Curr Biol *10*, 595-598.

Rusak, B., and Groos, G. (1982). Suprachiasmatic stimulation phase shifts rodent circadian rhythms. Science *215*, 1407-1409.

Seabrook, T.A., Burbridge, T.J., Crair, M.C., and Huberman, A.D. (2017). Architecture, Function, and Assembly of the Mouse Visual System. Annu Rev Neurosci *40*, 499-538.

Seth, A., Culverwell, J., Walkowicz, M., Toro, S., Rick, J.M., Neuhauss, S.C., Varga, Z.M., and Karlstrom, R.O. (2006). belladonna/(lhx2) is required for neural patterning and midline axon guidance in the zebrafish forebrain. Development *133*, 725-735.

Slavotinek, A.M., Chao, R., Vacik, T., Yahyavi, M., Abouzeid, H., Bardakjian, T., Schneider, A., Shaw, G., Sherr, E.H., Lemke, G.*, et al.* (2012). VAX1 mutation associated with microphthalmia, corpus callosum agenesis, and orofacial clefting: the first description of a VAX1 phenotype in humans. Hum Mutat *33*, 364-368.

Sloane, S.A., Shea, S.L., Procter, M.M., and Dewsbury, D.A. (1978). Visual cliff performance in 10 species of muroid rodents. Anim Learn Behav *6*, 244-248.

Soria, J.M., Taglialatela, P., Gil-Perotin, S., Galli, R., Gritti, A., Verdugo, J.M., and Bertuzzi, S. (2004). Defective postnatal neurogenesis and disorganization of the rostral migratory stream in absence of the Vax1 homeobox gene. J Neurosci *24*, 11171-11181.

Szabadi, E. (2018). Functional Organization of the Sympathetic Pathways Controlling the Pupil: Light-Inhibited and Light-Stimulated Pathways. Front Neurol *9*, 1069.

Tao, C., and Zhang, X. (2014). Development of astrocytes in the vertebrate eye. Dev Dyn *243*, 1501-1510.

Vacik, T., Stubbs, J.L., and Lemke, G. (2011). A novel mechanism for the transcriptional regulation of Wnt signaling in development. Genes Dev *25*, 1783-1795.

Wang, Y., Sabbagh, M.F., Gu, X., Rattner, A., Williams, J., and Nathans, J. (2019). Beta-catenin signaling regulates barrier-specific gene expression in circumventricular organ and ocular vasculatures. eLife *8*.

Williams, R.W., Hogan, D., and Garraghty, P.E. (1994). Target recognition and visual maps in the thalamus of achiasmatic dogs. Nature *367*, 637-639.

Williams, S.E., Grumet, M., Colman, D.R., Henkemeyer, M., Mason, C.A., and Sakurai, T. (2006). A role for Nr-CAM in the patterning of binocular visual pathways. Neuron *50*, 535-547.

Williams, S.E., Mann, F., Erskine, L., Sakurai, T., Wei, S., Rossi, D.J., Gale, N.W., Holt, C.E., Mason, C.A., and Henkemeyer, M. (2003). Ephrin-B2 and EphB1 mediate retinal axon divergence at the optic chiasm. Neuron *39*, 919-935.

Wolman, D. (2012). The split brain: a tale of two halves. Nature *483*, 260-263.

Yilmaz, M., and Meister, M. (2013). Rapid innate defensive responses of mice to looming visual stimuli. Curr Biol *23*, 2011-2015.

Zee, D.S. (1986). Brain stem and cerebellar deficits in eye movement control. Trans Ophthalmol Soc U K *105*, 599-605.

Zhang, C., Kolodkin, A.L., Wong, R.O., and James, R.E. (2017). Establishing Wiring Specificity in Visual System Circuits: From the Retina to the Brain. Annu Rev Neurosci *40*, 395-424.

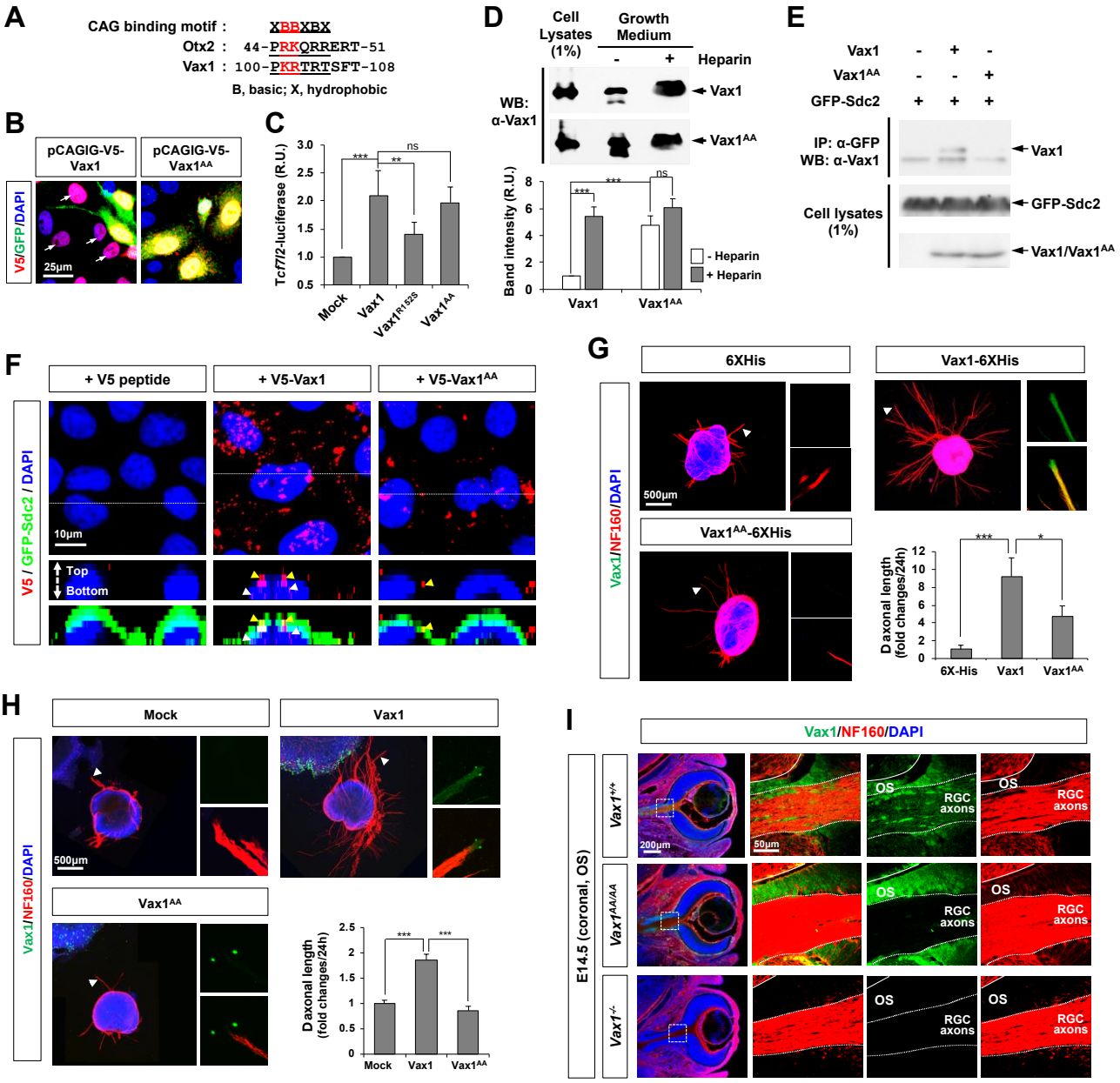

Figure 1. Identification a CAG sugar binding motif of Vax1. (**A**) Consensus amino acid sequences of GAG sugar-binding motifs in mouse Otx2 and Vax1. (**B**) Expression of V5-Vax1 and EGFP, which are independently translated from a same transcript, was examined by immunostaining of transfected HeLa cells with mouse anti-V5 (red) and chicken anti-GFP (green) antibodies. Arrows point HeLa cells express V5-Vax1 without EGFP, implicating the transfer of V5-Vax1 but not EGFP from V5;EGFP double-positive cells. (**C**) HEK293T cells were transfected with a DNA vector encodes Vax1, Vax1(R152S), or Vax1(KR/AA) cDNA together with a Vax1 target *Tcf7l2*-luciferase reporter DNA construct. Luciferase activities in the transfected cells were measured at 24-

h post-transfection. The values are average obtained from four independent experiments and error bars denote standard deviations (SD). *p*-values were determined by ANOVA test (*, p<0.01; **, p<0.005; ***, p<0.001; ns, not significantly different). (**D**) V5-tagged Vax1 or Vax1^{AA} proteins were expressed in HEK293T cells, and growth media of the transfected cells were then collected after incubating for 3h in the presence (+) or absence (-) of heparin (10 mg/ml final; see Methods for details). Cell lysates and TCA-precipitated fractions of growth medium were analyzed by 10% SDS-PAGE and subsequent western blotting (WB) with anti-Vax1 antibody (α-Vax1). A graph below the WB data shows the relative intensities of Vax1 bands in the blots. The values are average obtained from four independent experiments and error bars denote SD. (**E**) Interactions of V5-Vax1 and V5-Vax1^{AA} with GFP-Sdc2 in HEK293T cells were assessed by immunoprecipitation (IP) with α-V5 and subsequent WB with α-GFP. Relative amounts of V5-Vax1 and GFP-Sdc2 in the cell lysates were also examined by WB. (**F**) V5-Vax1 or V5-Vax1^{AA} recombinant proteins were added into growth medium of HeLa cells expressing GFP-Sdc2 and incubated for 3 h. Vax1 proteins inside cells and/or at the cell surface were detected by immunostaining with mouse α-V5 (red) and chick α-GFP (green). **(G)** Retinas were isolated from E13.5 mice and cultured as described in Methods. Axonal lengths of retinal explants were measured at 24 h post-culture; then, the explants were treated with 6X-His-tagged recombinant Vax1 or Vax1^{AA} proteins. **(H)** Alternatively, retinal explants were co-cultured with HEK293T cells transfected with pCAGIG (Mock), pCAGIG-V5-Vax1, or pCAGIG-V5-Vax1^{AA}. Axonal lengths were re-measured after 24 h and the explants were immunostained with α-Vax1 (green) and α-NF160 (red). Arrowheads indicate the areas magnified in each inset. The changes in axonal length during the 24-h incubation period were shown in graphs. The values in the graph are averages and error bars denote SDs (n=6). **(I)** Intercellular transfer of Vax1 from E14.5 *Vax1*$^{+/+}$ and *Vax1*$^{AA/AA}$ littermate mouse OS cells to RGC axons was determined by immunostaining of the embryonic sections with α-Vax1 (green) and α-NF160 (red). The solid lines in the images indicate the boundary of OS, and the dotted-lines mark the border between the OS and RGC axon bundles.

Min et al._Fig2

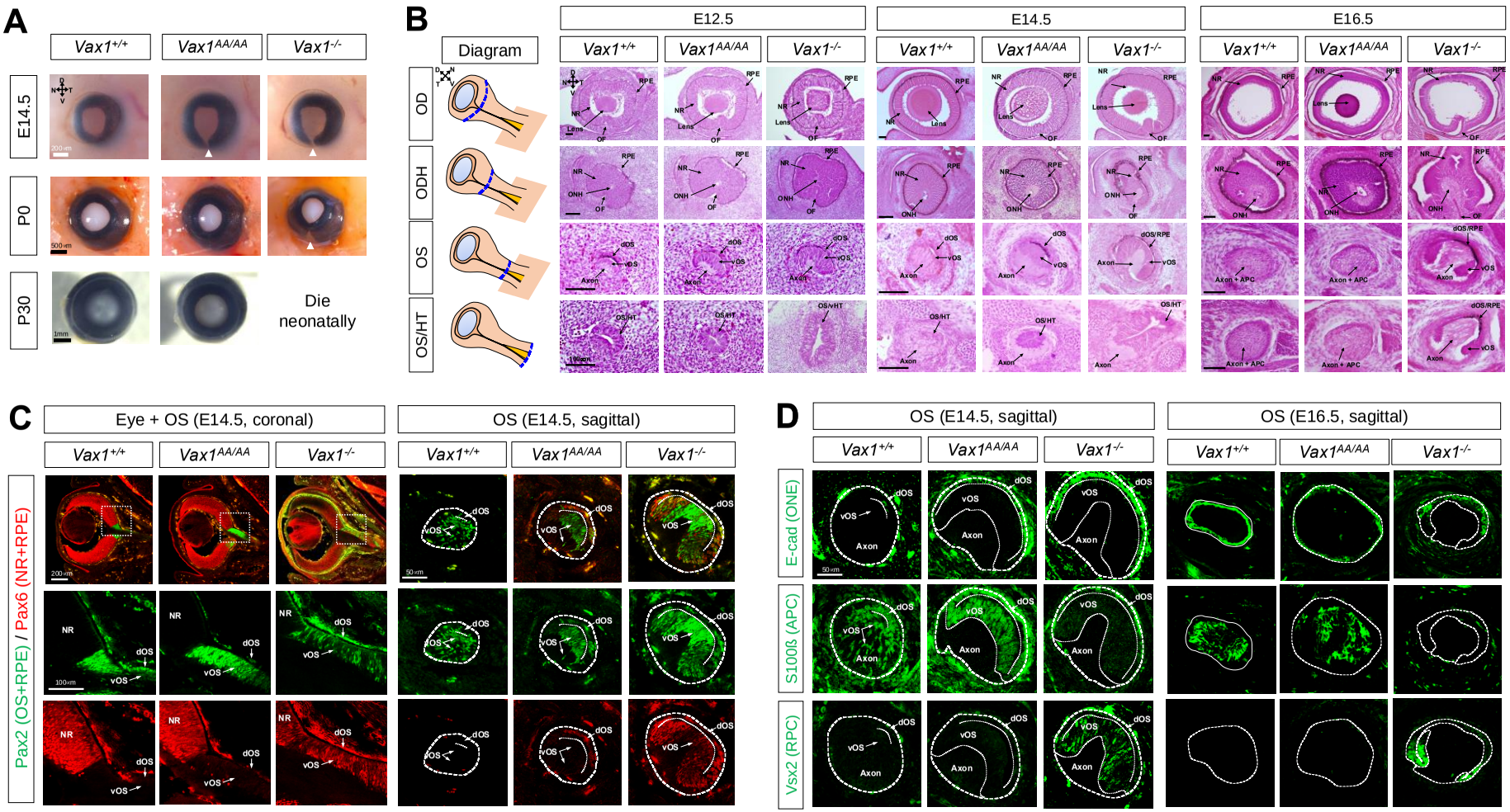

Figure 2. Developmental delay of OS differentiation in *Vax1*$^{AA/AA}$ mice. (A) Pictures of mouse eyes (frontal view) with the indicated genotypes are taken at various developmental stages. Arrowheads point the optic fissures. N, nasal; T, temporal; D, dorsal; V, ventral. **(B)** Sagittal sections of mouse embryos were stained with hematoxylin & eosin (H&E). Positions of the sections are indicated by blue plates in the diagram (leftmost column). APC, astrocyte precursor cell; ODH, optic disc head; OF, optic fissure; dOS, dorsal optic stalk; vOS, NR, neural retina; RPE, retinal pigment epithelium; ventral optic stalk; vHT, ventral hypothalamus. Scale bars in the pictures are 100 μm. **(C)** Distributions of Pax6 and Pax2 in E14.5 mouse embryonic sections were examined by immunostaining. Boxed areas in top row images of coronal sections are magnified in two bottom rows. **(D)** Sagittal sections including medial OS of E14.5 and E16.5 mouse embryos were stained with the antibodies recognized the corresponding markers. APC, astrocyte precursor cell; ONE, optic neuroepithelium; RPC, retinal progenitor cell.

Min et al._Fig3

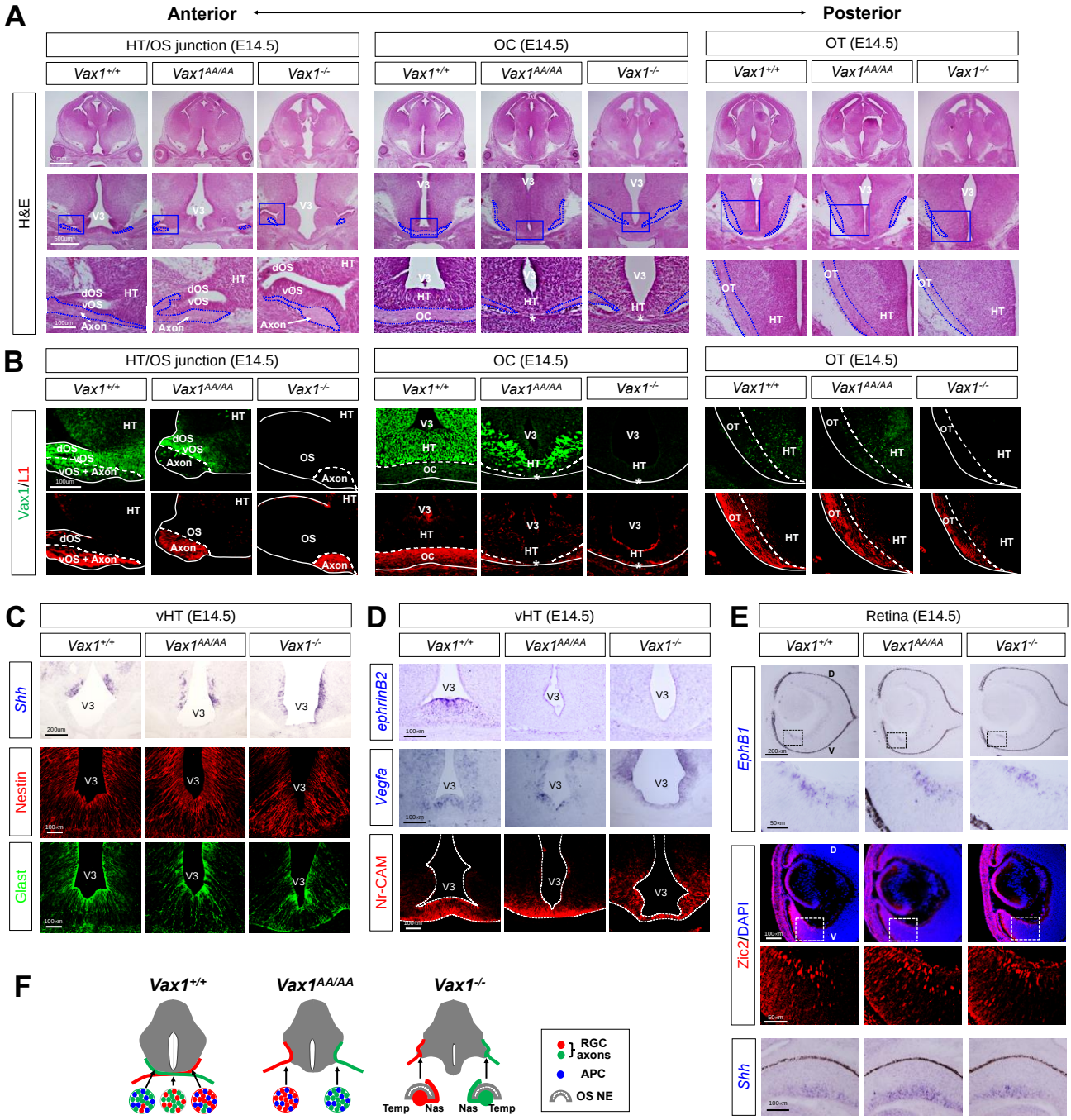

Figure 3. Agenesis of OC in *Vax1*$^{AA/AA}$ mice. (**A**) Coronal sections of E14.5 mouse embryos were stained with H&E. *, ventral midline of HT equivalent to the position of OC in *Vax1*$^{+/+}$ littermates. V3, third ventricle. (**B**) The sections were also immunostained with the antibodies recognize Vax1 (green) and an RGC axon marker, L1-CAM (L1, red). **(C)** Distributions of *Shh* mRNA in the embryonic sections were detected by *in situ* hybridization (ISH). Development of hypothalamic radial glia (RG) from NPC was determined by immunostaining for an RG marker Glast (glutamate aspartate transporter 1) and an NPC marker Nestin, respectively. **(D)** Expression of a repulsive guidance cue, ephrinB2, and the attractive guidance cues, Vegfa and Nr-CAM, for RGC axons in E14.5 mouse vHT was examined by *ISH* (*ephrin B2* and *Vegfa*) and IHC (Nr-CAM). **(E)** Expressions of retinal genes that induce ipsilateral RGC axon projection were examined by ISH (*EphB1* and *Shh*) and IHC (Zic2). Boxed areas in top row images are magnified in bottom rows. **(F)** Schematic diagrams that show the structures of OS/vHT junctions and RGC axon pathways in *Vax1*$^{+/+}$, *Vax1*$^{AA/AA}$, and *Vax1*$^{-/-}$ mice. Nas, nasal; Temp, temporal. OS NE, OS neuroepithelium.

Min et al._Fig4

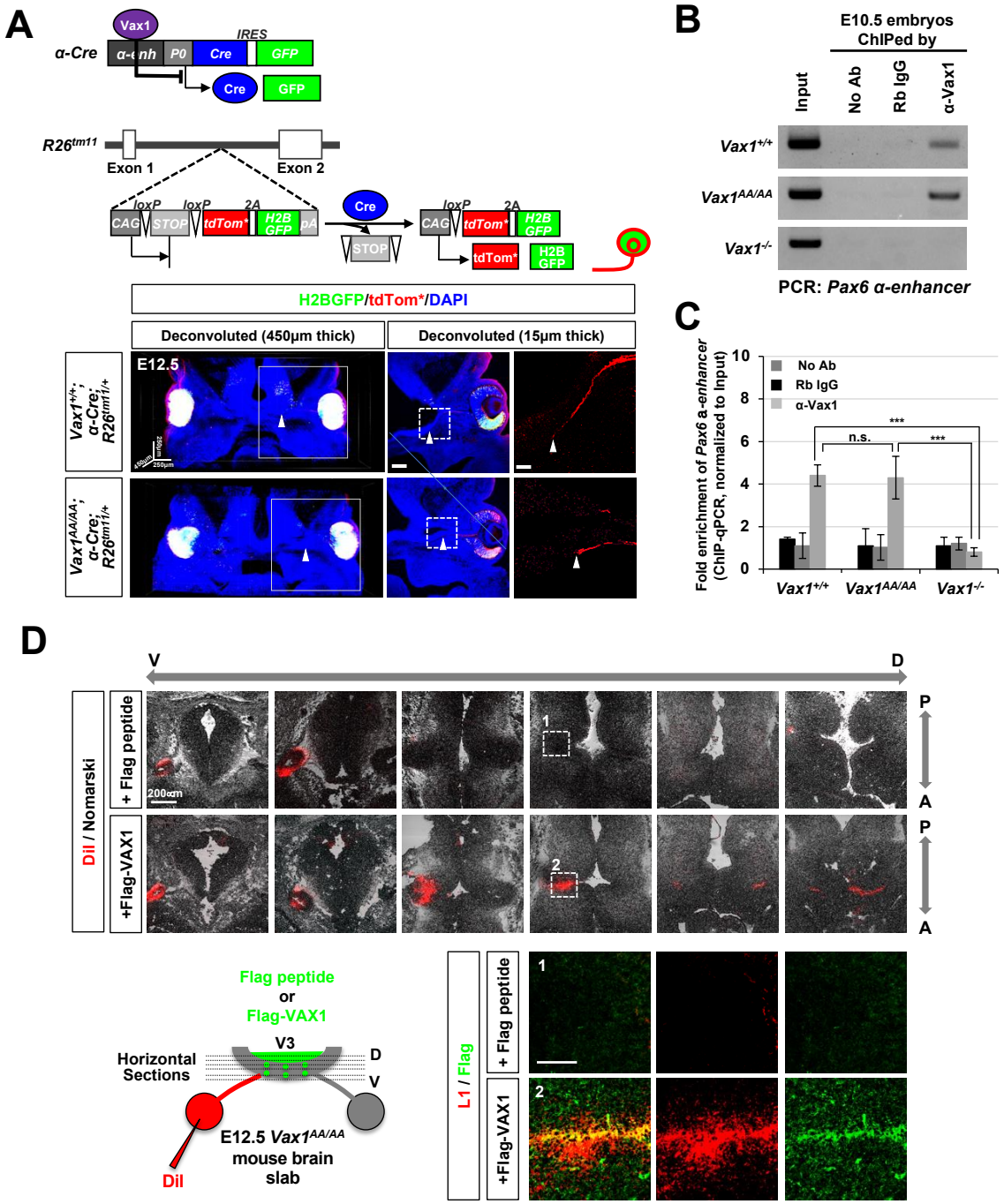

Figure 4. Regulation of RGC axon growth by Vax1 transfer. (A) The activities of a Vax1 target *Pax6 α-enhancer* in mouse embryos were measured by detecting H2B-EGFP, of which expression is induced together with membrane bound tdTomato (tdTom*) at *R26*^{tm11} gene locus after α-Cre-dependent excision of *loxP-STOP-loxP* cassette. Arrow heads point the frontlines of the RGC axons. **(B)** Binding of Vax1 and Vax1^{AA} proteins on the *Pax6 α-enhancer* was determined by PCR detection of *Pax6 α-enhancer* sequences in DNA fragments isolated from E10.5 mouse embryonic cells by ChIP with indicated antibodies (see details in Methods). Input, mouse chromosomal DNA; No Ab, no antibody; Rb IgG, preimmune rabbit IgG; α-Vax1, rabbit anti-Vax1 polyclonal antibody. **(C)** Relative levels of *Pax6 α-enhancer* sequences in the ChIPed samples were compared by qPCR. The numbers in y-axis are average $2^{-\Delta Ct}$ values of the samples against critical threshold (Ct) values of Input. Error bars denote SD (n=5). **(D)** Collagen beads soaked with Flag peptides or Vax1-Flag protein were implanted in the third ventricle of E12.5 *Vax1*$^{AA/AA}$ mouse embryonic brain slabs, while DiI fluorescent dye was filled in their right eyes (diagram). Distribution of DiI-labeled RGC axons in the horizontal sections of brain slabs were then visualized after 12h (i.e., E13). The penetration of Vax1-Flag proteins into RGC axons were confirmed by co-immunostaining with anti-Flag and anti-L1-CAM antibodies.

1035

Min et al._Fig5

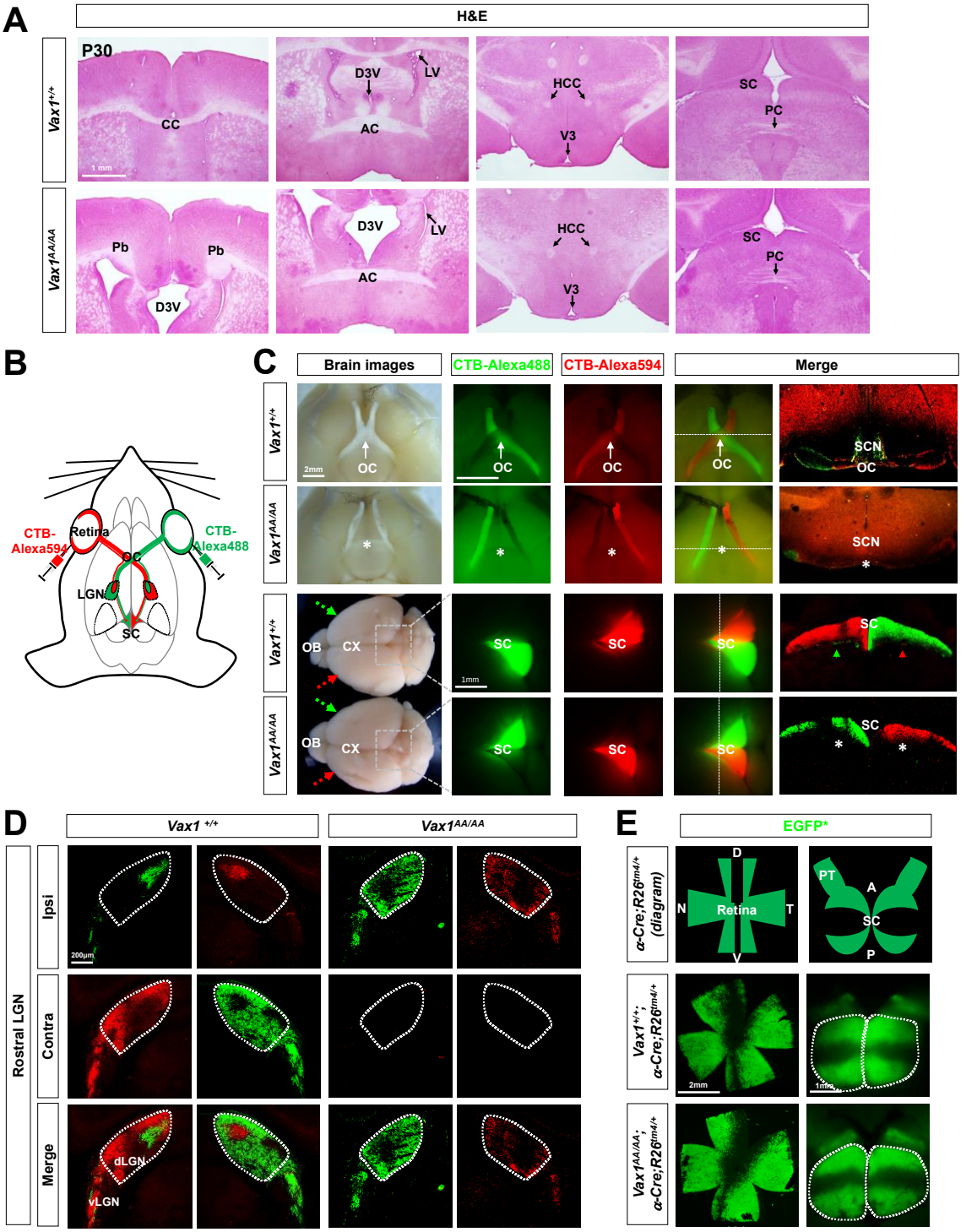

1036

1037

Figure 5. Ipsilaterally-biased RGC axon projection in *Vax1*$^{AA/AA}$ mice. (A) Coronal sections of P30 mouse brain were stained with H&E. The sections containing the indicated commissural structures were identified and shown. AC, anterior commissure; CC, corpus callosum; D3V, dorsal third ventricle; HCC, hypothalamic cell cord; Pb, probus bundle; PC, posterior commissure; SC, superior colliculus. **(B)** Diagram depicts fluorescence labeling of mouse RGCs. **(C)** Alexa488- and Alexa594-labeld CTB proteins were injected into right and left eyes of the mice at P28, respectively. Brains of the CTB-injected mice were isolated at P30 and fluorescent signals emitted from the brains were visualized by Axio Zoom stereoscope (Zeiss; three center columns), and then the fluorescent signals in coronal sections of the brains were detected by FV1000 confocal microscope (Olympus; rightmost column). Bright-field images of the brains were also taken to show the structure of the brains and optic nerves (leftmost column). CX, cerebral cortex; OB, olfactory bulb; *, ventral midline of HT equivalent to the position of OC in *Vax1*$^{+/+}$ littermates. **(D)** Coronal sections of the CTB-injected mouse brains were collected and fluorescent signals in the LGN area were detected. The areas surrounded by dotted lines are dLGN. Contra, contralateral LGN section; Ipsi, ipsilateral LGN section. **(E)** The retinas and brains of P30 *Vax1*$^{+/+}$ and *Vax1*$^{AA/AA}$ littermate mice carrying α-*Cre*;*R26*$^{tm4/+}$ transgenes, which express membrane-targeted EGFP (EGFP*) at *R26*^{tm4} gene locus upon Cre-dependent excision of *loxP-tdTomato*-loxP* gene cassette, were isolated and visualized. The areas surrounded by dotted lines are SC. PT, pretectum.

1060

1061

1062

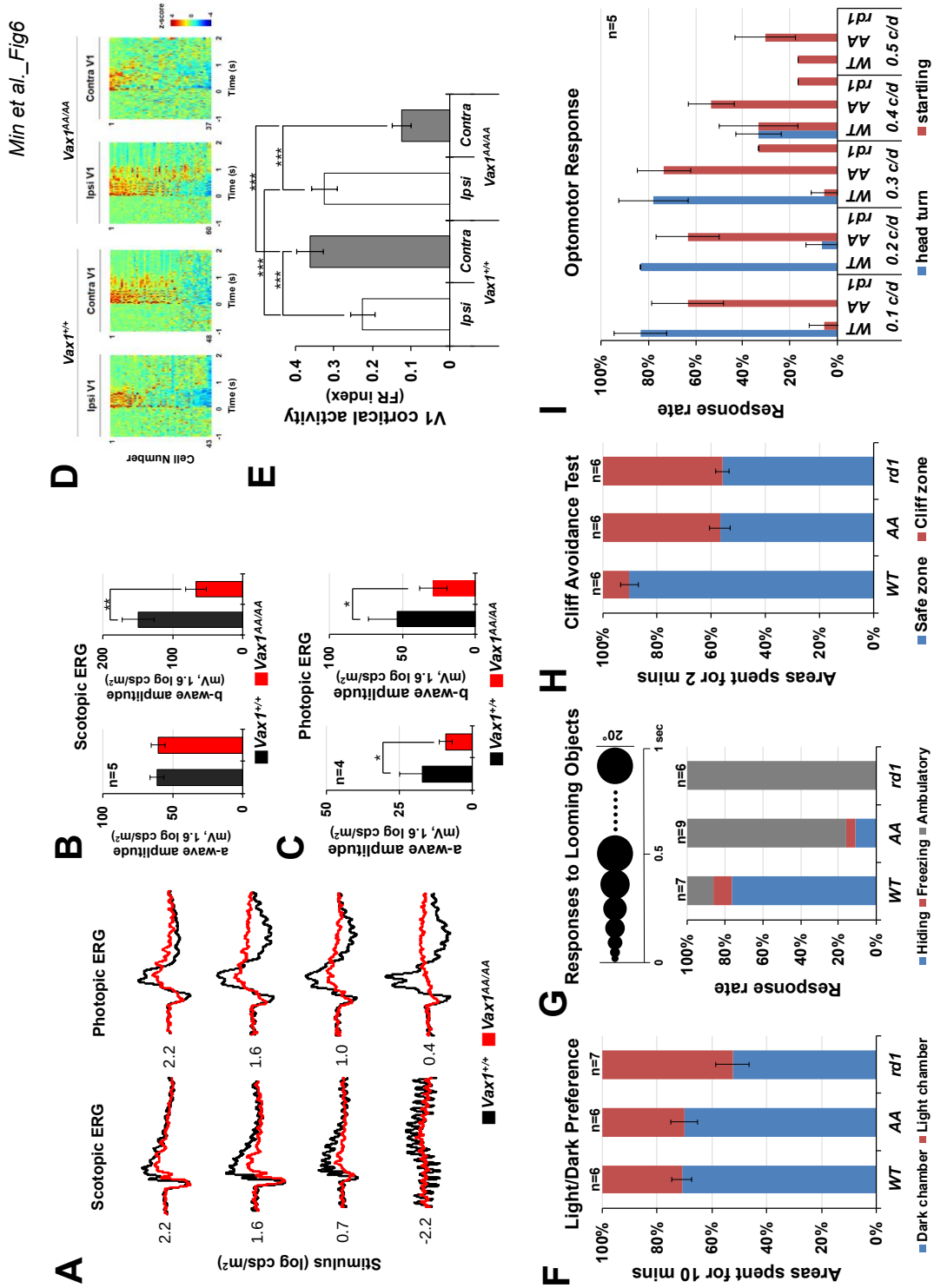

Figure 6. Reduced visual acuity of *Vax1*$^{AA/AA}$ mice. (A) Electrophysiological activities of P45 *Vax1*$^{+/+}$ and *Vax1*$^{AA/AA}$ mouse retinas were examined by ERG (see details in Methods). The amplitudes of scotopic **(B)** and photopic **(C)** ERG a- and b-waves at 1.6 log cds/m^2 condition are presented. Numbers of mice tested are given in the graphs (4 independent litters). **(D)** Light-evoked excitation of cortical neurons in P45 *Vax1*$^{+/+}$ and *Vax1*$^{AA/AA}$ mouse V1 were measured by silicon multielectrode probes after monocular illumination (see details in Methods). Responses of neurons in the monocular zones of ipsilateral (Ipsi) and contralateral (Contra) visual cortices were recorded. Color-coded heatmap represents average z-scores of spike firing rates. Red indicates increase and blue indicates decrease of firing rates from the baseline, respectively. **(E)** Mean firing-rate change index of ipsilateral and contralateral V1 neurons in *Vax1*$^{+/+}$ and *Vax1*$^{AA/AA}$ mice. y-axis values are mean ± SEM. **(F)** Relative occupancy of light and dark chambers by P45 *Vax1*$^{+/+}$ (*WT*), *Vax1*$^{AA/AA}$ (*AA*), and *Pde6b*$^{rd1/rd1}$ (*rd1*) mice for 10-min measurement period was determined and shown in a graph. **(G)** Escaping responses of the mice, which were given the expanding black circle on top screens to mimic a looming shadow of predator, were determined and shown in a graph. **(H)** To determine stereoscopic vision of the mice, relative occupancy of safe and cliff zones by the mice for 2-min measurement period was determined and shown in a graph. **(I)** Accuracy of the mice to turn their heads to the directions where black and white vertical stripes rotate was measured and shown in a graph (head turn). Startling responses of the mice in response to the stimuli was also measured (startling). Numbers of the mice tested are given in the graphs in F – H.

Min et al._Fig7

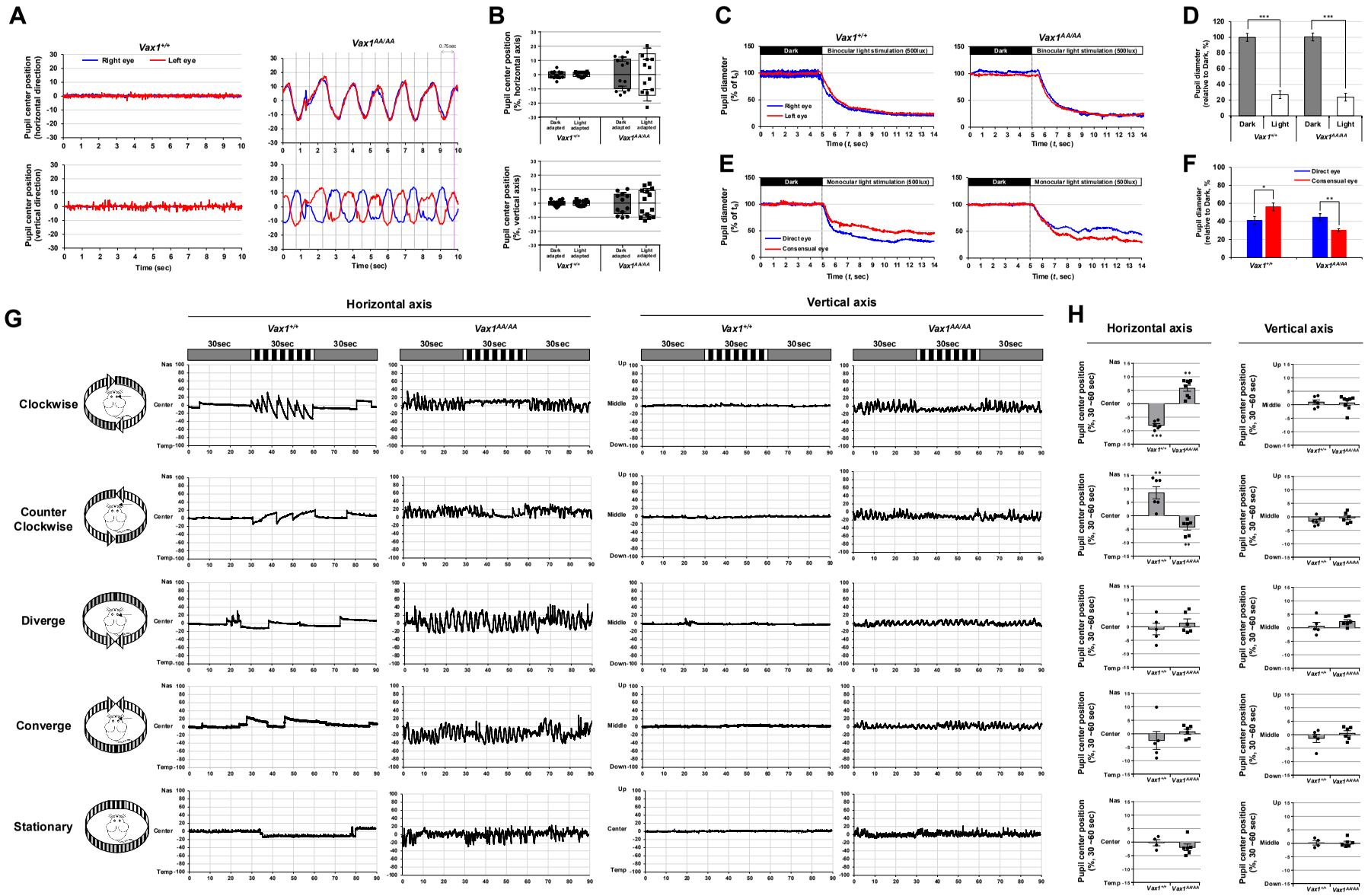

Figure 7. Inversed oculomotor responses of *Vax1*$^{AA/AA}$ mice. (A) Positions of pupil centers in right and left eyes of head-fixed P45 *Vax1*$^{+/+}$ and *Vax1*$^{AA/AA}$ mice were tracked by the iSCAN rodent eye tracking system while the mice were kept in dark. Relative positions of pupil centers against the position at time 0 (t_0) were plotted in the oscillograms. **(B)** Peak positions that the pupil centers moved at vertical and horizontal axes are measured and the averages are shown in graphs. Error bars are SD (n=6). **(C)** The P45 mice were adapted in dark for 30 mins and illuminated with room light. **(E)** Alternatively, the dark-adapted mice were illuminated monocularly with a point light. Pupil diameters were measured by iSCAN eye tracking system before and after the illuminations. Relative pupil diameters against t_0 are plotted in oscillograms. **(D** and **F)** Average pupil diameters of the mice in dark (t_0 ~ t_5) and light (t_5 ~ t_{14}) conditions are measured and shown in graphs. Error bars are SD (n=6 [*Vax1*$^{+/+}$] and n=7 [*Vax1*$^{AA/AA}$]). *, $p<0.05$; **,$p<0.01$; ***, $p<0.005$. **(G)** Head-fixed P45 *Vax1*$^{+/+}$ and *Vax1*$^{AA/AA}$ mice were positioned in a chamber surrounded by monitors, which display gray background. Center positions of the pupils in right and left eyes were marked and then tracked by the iSCAN rodent eye tracking system while the mice were exposed to the monitors display black and white vertical stripes (0.2 c/d), which are moving in the indicated directions for 30 seconds. Relative positions of pupil centers of right eyes against the position at t_0 are plotted in the oscillograms. Peak positions of the pupil centers between 30 sec and 60 sec at horizontal **(H)** and vertical **(I)** axes were collected, and the averages are shown in graphs. Error bars are SD (n=6 [*Vax1*$^{+/+}$] and n=8 [*Vax1*$^{AA/AA}$]).

Supplemental Information

Figure S1. Generation of *Vax1*$^{AA/AA}$ mice.
Figure S2. Anatomical features of retina and optic nerve in *Vax1*$^{AA/AA}$ mice.
Figure S3. Spontaneous oscillation of *Vax1*$^{AA/AA}$ mouse eyes.
Table S1. List of antibodies used in this study.
Movie S1. Response of *Vax1*$^{+/+}$ mice to a looming shadow.
Movie S2. Response of *Vax1*$^{AA/AA}$ mice to a looming shadow.
Movie S3. Response of *Pde6b*$^{rd1/rd1}$ mice to a looming shadow.
Movie S4. Cliff assay of *Vax1*$^{+/+}$ mice.
Movie S5. Cliff assay of *Vax1*$^{AA/AA}$ mice.
Movie S6. Cliff assay of *Pde6b*$^{rd1/rd1}$ mice.
Movie S7. Optomotor response of *Vax1*$^{+/+}$ mice.
Movie S8. Optomotor response of *Vax1*$^{AA/AA}$ mice.
Movie S9. Optomotor response of *Pde6b*$^{rd1/rd1}$ mice.
Movie S10. Eye movement of *Vax1*$^{+/+}$ mice in dark.
Movie S11. Eye movement of *Vax1*$^{AA/AA}$ mice in dark.
Movie S12. Pupil contraction of *Vax1*$^{+/+}$ mice after binocular light illumination.
Movie S13. Pupil contraction of *Vax1*$^{AA/AA}$ mice after binocular light illumination.
Movie S14. Pupil contraction of *Vax1*$^{+/+}$ mice after monocular light illumination.
Movie S15. Pupil contraction of *Vax1*$^{AA/AA}$ mice after monocular light illumination.
Movie S16. Eye movement of *Vax1*$^{+/+}$ mice in response to vertical stripes rotating clockwise direction.
Movie S17. Eye movement of *Vax1*$^{AA/AA}$ mice in response to vertical stripes rotating clockwise direction.
Movie S18. Eye movement of *Vax1*$^{+/+}$ mice in response to vertical stripes rotating counter clockwise direction.
Movie S19. Eye movement of *Vax1*$^{AA/AA}$ mice in response to vertical stripes rotating counter clockwise direction.
Movie S20. Eye movement of *Vax1*$^{+/+}$ mice in response to converging vertical stripes.
Movie S21. Eye movement of *Vax1*$^{AA/AA}$ mice in response to converging vertical stripes.
Movie S22. Eye movement of *Vax1*$^{+/+}$ mice in response to diverging vertical stripes.
Movie S23. Eye movement of *Vax1*$^{AA/AA}$ mice in response to diverging vertical stripes.
Movie S24. Eye movement of *Vax1*$^{+/+}$ mice in response to stationary vertical stripes.
Movie S25. Eye movement of *Vax1*$^{AA/AA}$ mice in response to stationary vertical stripes.

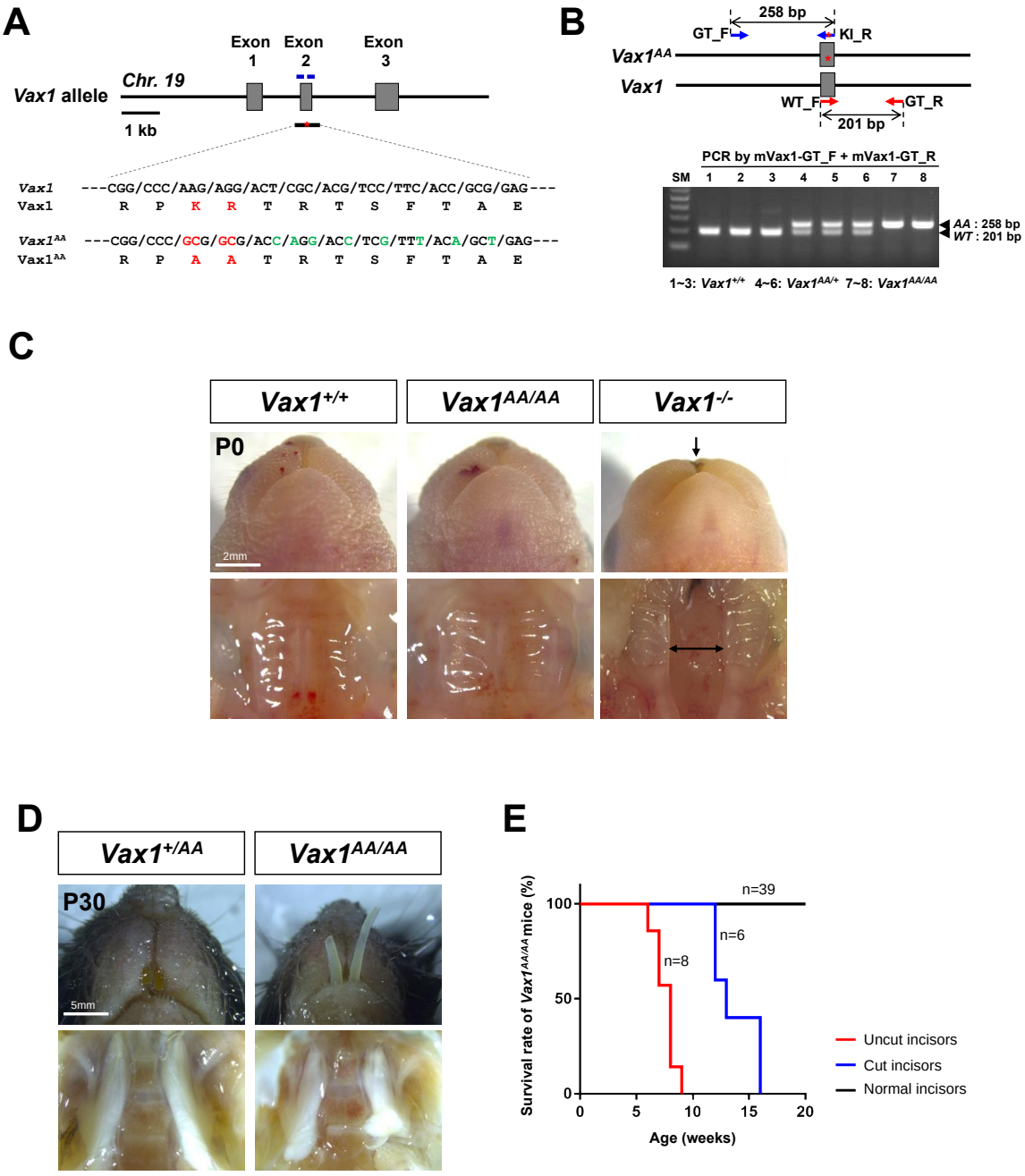
A
Exon 1
Exon 2
Exon 3
Vax1 allele
Chr. 19
1 kb
Vax1 ---CGG/CCC/AAG/AGG/ACT/CGC/ACG/TCC/TTC/ACC/GCG/GAG---
Vax1 R P K R T R T S F T A E
Vax1AA ---CGG/CCC/GCG/GCG/ACC/AGG/ACC/TCG/TTT/ACA/GCT/GAG---
Vax1AA R P A A T R T S F T A E
B
258 bp
GT_F
KI_R
Vax1AA
Vax1
WT_F
GT_R
201 bp
PCR by mVax1-GT_F + mVax1-GT_R
SM 1 2 3 4 5 6 7 8
AA : 258 bp
WT : 201 bp
1~3: Vax1+/+ 4~6: Vax1AA/+ 7~8: Vax1AA/AA
C
Vax1+/+
Vax1AA/AA
Vax1-/-
P0
2mm
D
Vax1+/AA
Vax1AA/AA
P30
5mm
E
Survival rate of Vax1AA/AA mice (%)
100
50
0
0 5 10 15 20
Age (weeks)
n=39
n=6
n=8
Uncut incisors
Cut incisors
Normal incisors

Figure S1. Generation of *Vax1*$^{AA/AA}$ mice. (**A**) Structure of mouse *Vax1*^{AA} gene (top) and its partial sequences of exon 2 that encode AA replacing KR in the GAG binding motif (bottom). The substituted nucleotides for missense (red, KR to AA) and synonymous (green) mutations are shown. The amino acid sequences from the Vax1 and the Vax1^{AA} alleles are shown at the bottom of each nucleotide sequence. The relative positions of two crRNAs and ssODN are indicated in short blue bars and black bar with asterisk (*), respectively. (**B**) Top, relative positions of genotyping primers are indicated by arrows. The red asterisks (*) indicate KR to AA mutation. Bottom, PCR genotyping results using genotyping primers. (**C**) Ventral views of P0 mouse mouths (top) and palates (bottom). Arrows indicate the clefts of lip (top) and palate (bottom), respectively. (**D**) Ventral views of P30 mouse mouths (top) and palates (bottom). (**E**) Survival rates of *Vax1*$^{AA/AA}$ mice by the indicated ages in x-axis are provided. Numbers of mice examined were provided in the graph.

Figure

features

and

in

mice.

views of

P30

littermate

sections

nerves of

and

littermate

stained

Oil Red-

visualize

cells and

nerves,

The

were

Min et al._FigS2

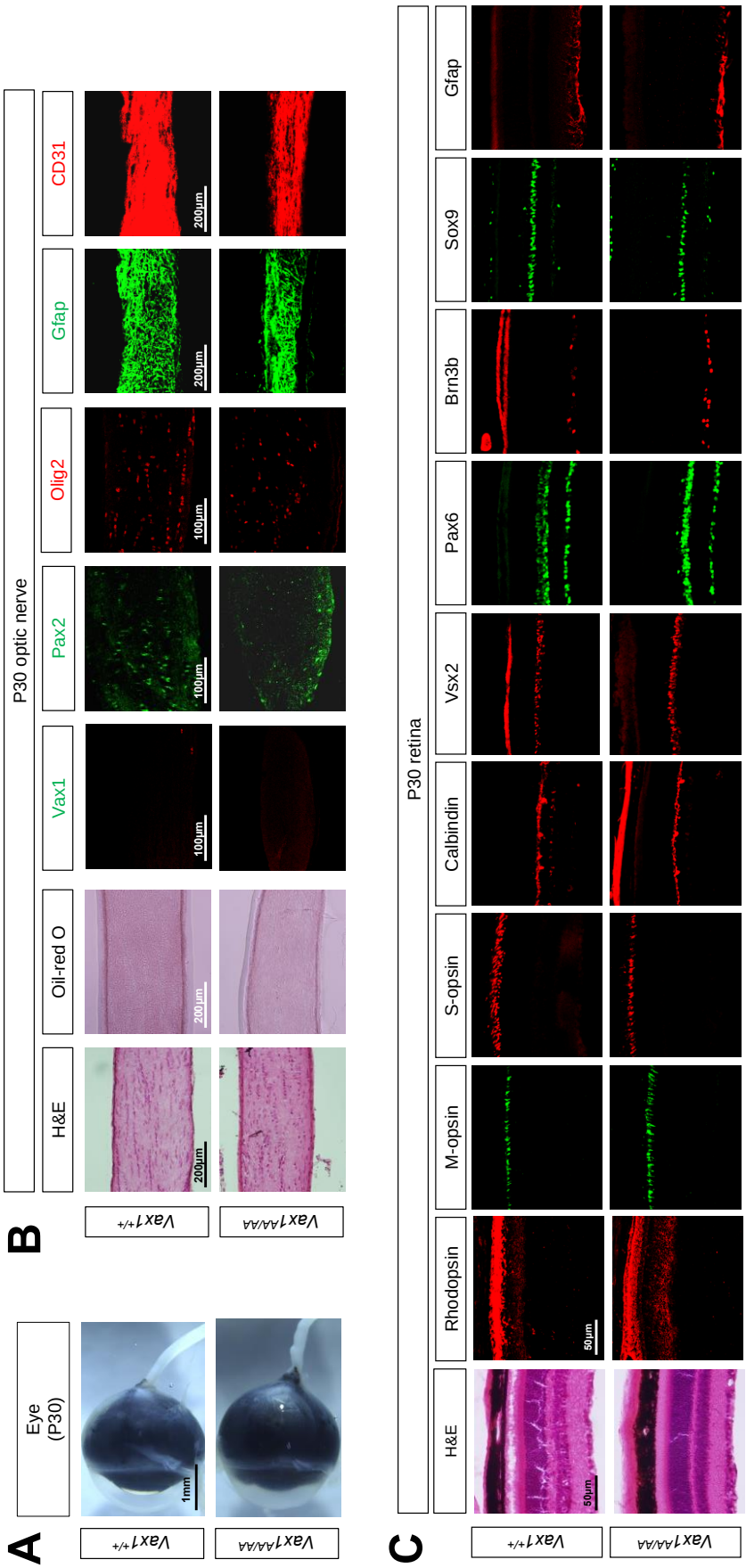

S2.

Anatomical

of retina

optic nerve

Vax1$^{AA/AA}$

(**A**) Lateral

the eyes of

Vax1$^{+/+}$ and

Vax1$^{AA/AA}$

mice. (**B**)

Longitudinal

of optic

P30 *Vax1$^{+/+}$*

Vax1$^{AA/AA}$

mice were

by H&E and

O to

the

distribution of

lipids in the

respectively.

sections

also

immunostained with the antibodies that recognize the indicated marker proteins. Pax2 and Gfap, astrocytes; CD31, endothelial cells; Olig2, oligodendrocytes. Vax1 is not expressed in the adult optic nerves. (**C**) Sections of the eyes of P30 *Vax1*$^{+/+}$ and *Vax1*$^{AA/AA}$ littermate mice were stained by H&E or the antibodies that recognize the indicated marker proteins. Rhodopsin, rod photoreceptors; M-opsin, M-cone photoreceptors; S-opsin, S-cone photoreceptors; Calbindin, horizontal and amacrine cells; Vsx2, bipolar cells; Pax6, amacrine cells; Brn3b, RGCs; Sox9, Müller glia; Gfap, astrocytes.

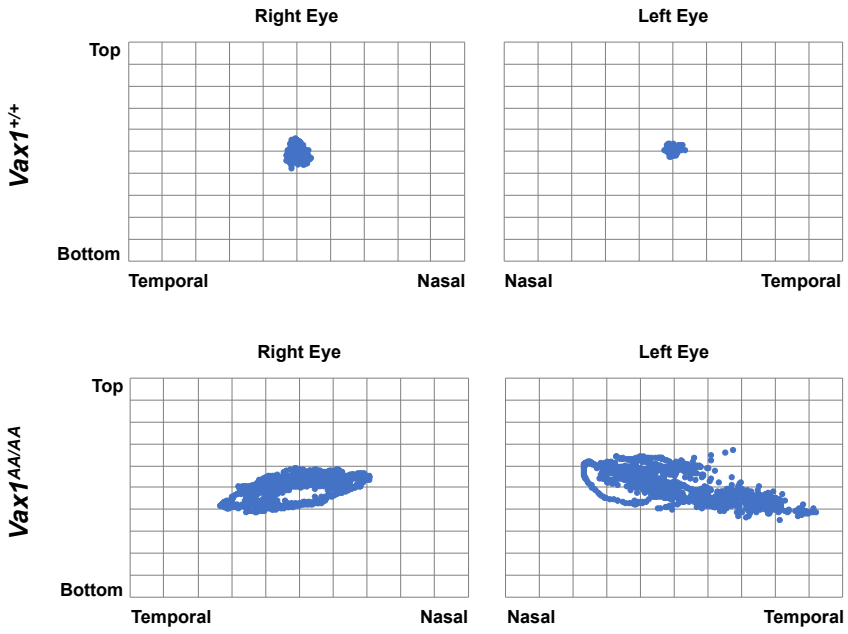

Figure S3. Spontaneous movement of *Vax1*$^{AA/AA}$ mouse eyes. Relative positions of the pupils in right and left eyes of head-fixed P45 *Vax1*$^{+/+}$ and *Vax1*$^{AA/AA}$ were recorded by the iSCAN rodent eye tracking system at every 8 msec for 10 secs while the mice were kept in dark. The positions were plotted in the graphs. The results show the eyes of *Vax1*$^{AA/AA}$ rotate spontaneously in an oval track while *Vax1*$^{+/+}$ mouse eyes keep their positions in dark.

Table S1. Antibodies used in this study

Antigen	Origin	Dilution	Maker	Catalog #
b-actin	Rabbit	1:1000	Santa cruz biotechnology	SC-1616
Brn3b	Goat	1:200	Santa cruz biotechnology	SC-31989
CD31	Hamster	1:200	Millipore	MAB1398Z
E-cad	Mouse	1:200	BD	610181
GFAP	Rabbit	1:200	Abcam	AB48050
GFP	Rabbit	1:200	Abcam	AB290
GFP	Mouse	1:200	Santa cruz biotechnology	SC-9996
Glast	Guinia pig	1:500	Millipore	AB1782
L1-CAM	Rat	1:200	Millipore	MAB5272
M-opsin	Mouse	1:200	Millipore	AB5405
Nestin	Mouse	1:100	Millipore	MAB353
NF160	Mouse	1:50	DSHB	2H3
Nr-CAM	Rabbit	1:200	Abcam	AB24344
Olig2	Rabbit	1:200	Millipore	AB9610
Pax2	Rabbit	1:200	Invitrogen	71-6000
Pax6	Rabbit	1:200	Covance	PRB-278P
Pax6	Mouse	1:200	Santa cruz biotechnology	SC-81649
Rhodopsin	Mouse	1:200	Chemicon	MAB5356
S-opsin	Rabbit	1:200	Millipore	AB5407
S100b	Rabbit	1:500	Abcam	AB52642
Sox9	Rabbit	1:200	Santa cruz biotechnology	SC-20095
Vax1	Rabbit	1:50	Mui et al. (2005)	N.A.
Vsx2	Guinia pig	1:200	gift from Dr. Mi-Ryoung Song (GIST)	N.A.
Zic2	Rabbit	1:200	Millipore	AB15392